Nanocrystalline Silicon Solar Cells Deposited via Pulsed PECVD at 150°C Substrate Temperature

by

K M Azizur Rahman

A thesis
presented to the University of Waterloo
in fulfillment of the
thesis requirement for the degree of
Master of Applied Science
in
Electrical and Computer Engineering

Waterloo, Ontario, Canada, 2010

Authors Declaration

I hereby declare that I am the sole author of this thesis. This is a true copy of the thesis, including any required final revisions, as accepted by my examiners.

I understand that my thesis may be made electronically available to the public.

Abstract

A series of experiments was carried out to compare the structural and electronic properties of intrinsic nanocrystalline silicon (nc-Si:H) thin films deposited via continuous wave (cw) and pulsed (p)-PECVD at 150°C substrate temperature. Working at this temperature allows for the easy transfer of film recipes from glass to plastic substrates in the future. During the p-PECVD process the pulsing frequency was varied from 0.2 to 50 kHz at 50% duty cycle. Approximately 15% drop in the deposition rate was observed for the samples fabricated in p-PECVD compared to cw-PECVD. The optimum crystallinity and photo (σ_{ph}) and dark conductivity (σ_D) were observed at 5 kHz pulsing frequency, with ~10% rise in crystallinity and about twofold rise in the σ_{ph} and σ_D compared to cw-PECVD.

However, for both the cw and p-PECVD nc-Si:H films, the observed σ_{ph} and σ_D were one to two orders and three orders of magnitude higher respectively than those reported in literature. The average activation energy (E_A) of 0.16 $\pm$ 0.01 eV for nc-Si:H films deposited using p-PECVD confirmed the presence of impurities, which led to the observation of the unusually high conductivity values. It was considered that the films were contaminated by the impurity atoms after they were exposed to air.

Following the thin film characterization procedure, the optimized nc-Si:H film recipes, from cw and p-PECVD, were used to fabricate the absorber layer of thin film solar cells. The cells were then characterized for J-V and External Quantum Efficiency (EQE) parameters. The cell active layer fabricated from p-PECVD demonstrated higher power conversion efficiency (η) and a maximum EQE of 1.7 $\pm$ 0.06 % and 54.3% respectively, compared to 1.00 $\pm$ 0.04 % and 48.6% respectively for cw-PECVD. However, the observed η and EQE of both the cells were lower than a reported nc-Si:H cell fabricated via p-PECVD with similar absorber layer thickness.

This was due to the poor Short-circuit Current Density (J_{sc}), Open-circuit Voltage (V_{oc}), and Fill Factor (FF) of the cw and p-PECVD cells respectively, compared to the reported cell. The low J_{sc} resulted from the poor photocarrier collection at longer and shorter wavelengths and high series resistance (R_{series}). On the other hand, the low V_{oc} stemmed from the low shunt resistance

(R_{sh}). It was inferred that the decrease in the R_{sh} occurred due to the inadequate electrical isolation of the individual cells and the contact between the n – layer and the front TCO contact at the edge of the p-i-n deposition area. Additionally, the net effect of the high R_{series} and the low R_{sh} led to a decrease in the FF of the cells.

Acknowledgements

All praises belong to God for giving me the intellectual ability, strength, and good health to progress this far in my education.

Thereafter, I would like to thank my supervisor, Professor Andrei Sazonov, for motivating me to pursue my Thesis topic, *Nanocrystalline Silicon Solar Cells Deposited via Pulsed PECVD at 150°C Substrate Temperature*. I would also like to thank Professor Siva Sivoththaman for being my acting supervisor in the absence of Professor Sazonov and my thesis reviewers, Professors Dyan Ban and C.R. Selvakumar.

I am greatly indebted to Professor Siva and Wendy Boles for overseeing my academic progress and financial arrangements, in the absence of my supervising professor, and allowing me to attend the MRS conference in San Francisco. Additionally, I am thankful to Professor Selvakumar for his valuable corridor discussions associated with my research. He along with my dear friends, Salman Kabir, Na'el Suwan, Michael M. Adachi, Rubayat Yameen and Dr. Shaikh Hasibul Majid, critically reviewed my MRS conference proceeding manuscript.

Special thanks to Professor Tong Leung and Samad Bazargan for their kind assistance with surface glancing XRD measurement, Randy Fagan for Raman Spectroscopy training and measurement, Ehsan Fathi for training me on the Reel to Reel (R-to-R) deposition system, Majid Gharghi for solar cell characterization measurements, and Kyung-Wook Shin and Richard Barbar for helping me with various instruments in the G2N lab.

I am also grateful to Michael and Majid for providing me valuable research tips and intellectually stimulating discussion on photovoltaics, Salman for keeping me company with his humorous exploits and motivating me to do extracurricular activities, Rubayat for theological discussions to keep me grounded, and each and every single one of my friends for their part in shaping my ideas.

Lastly, I do not think this acknowledgement section is complete without mentioning my parents, Dr. Mohammad Sanaullah and Mansura Begum, and siblings, K M Anisur Rahman and K M Abidur Rahman, for their unconditional support and sacrifice in helping me get this far.

Thank you all…

Dedication

To my Parents, Siblings, and Friends
for their patience and sacrifice

Table of Contents

List of Figures

List of Tables

Chapter 1: Introduction

Over the past couple of decades thin film silicon solar cells have garnered significant research interest from the PV community as a cheap alternative to crystalline silicon (c-Si) solar cells. Although its *power conversion efficiency* (**η**; 9.5 $\pm$ 0.3% [1] and 10.1 $\pm$ 0.2% [1] for stabilized amorphous silicon and nanocrystalline silicon solar cells respectively) is much lower than c-Si based cells (24.7 $\pm$ 0.5%), its unique material properties and fabrication process allows it to be fabricated over large areas at low deposition temperatures on different substrates [2]. This allows for the possibility of mass production through roll-to-roll processing [2].

Thin film silicon thickness ranges from couple of nanometers to several micrometers. It incorporates *hydrogenated amorphous silicon* (**a-Si:H**), *hydrogenated nano/micro-crystalline silicon* (**n/μc-Si:H**), and *hydrogenated polycrystalline silicon* (**poly-Si:H**) respectively (**Table 1.1**) [3]. The "hydrogenated" term in front of the thin film phase names are almost always omitted in device literature for shorthand purposes. This is because hydrogen plays an essential component in making these films device worthy and hence by omitting them in front of the phase names, implicitly implies a hydrogenated film.

Table 1.1: Different silicon thin films are defined based on their structural morphology [4]. Table adapted from reference [4].

Identification	Symbol	Phases	Feature Size
Hydrogenated amorphous silicon	a-Si:H	Single amorphous phase	–
Hydrogenated nano/micro – crystalline silicon	n/μc-Si:H	Composed of two phases (dual phase): amorphous and crystalline	< 20 nm crystalline grains
Hydrogenated polycrystalline silicon	poly-Si:H	Single crystalline phase with grain boundaries	> 20 nm for the smallest crystalline grains

Furthermore, nc-Si:H and μc-Si:H are synonymous phases. Initially this dual, amorphous and crystalline, phase was termed μc-Si:H [4]. This resulted from the observation of micron sized crystalline columns embedded in the amorphous matrix. However, over the past decade a shift in the naming convention, from μc-Si:H to nc-Si:H, was introduced. This culminated from various reports that the micron sized columns were a conglomerate of closely packed nanometer sized grains [3]. Hence, in this report this dual phase will be named nc-Si:H and all historical references for μc-Si:H will be identified as nc-Si:H. Additionally, since the focus of this report is nc-Si:H, the discussion from here on will only revolve around nc-Si:H and a-Si:H respectively. Moreover, thin film silicon solar cells are often named in terms of the phases used for the absorber layer. This naming convention will be used in this report as well.

nc-Si:H evolved out of the continuous research activity on a-Si:H. H. F. Sterling and R. C. G. Swann (1965), were the first to report a-Si:H thin film following the *radio frequency* (**rf**) *Plasma Enhanced Chemical Vapor Deposition* (**PECVD**) process [4]. But the deposited films were highly resistive [4]. Later, R. C. Chittick et al. (1969) deposited a-Si:H using the same deposition technique and found that the films had better photoconductive properties than those reported from other deposition methods, namely evaporation and sputtering [4-6]. They were also the first to report on the possibility of doping a-Si:H substitutionally.

Expanding on the aforementioned observation, W. E. Spear and P. G. LeComber (1975 – 1976), after a series of studies, were eventually able to deposit p and n-type a-Si:H from an admixture of silane and different doping gases [4, 5]. This was a major breakthrough in the field, since before they published their report, it was generally thought that a-Si:H could not be substitutionally doped [4]. In the same paper, they also investigated the film *dark conductivity* (**σ_D**) and the *Fermi energy level* (**E_F**) positioning under varying dopant concentrations [4, 5]. They reported that the σ_D of the *doped* (**extrinsic**) and *undoped* (**intrinsic**) films were far lower than c-Si [5]. Moreover, under heavy doping conditions the E_F only moved half way between the midgap and the respective band edges [5]. This occurs due to the rise in dopant induced defect density in the film [5]. Hence, it implies that the carrier diffusion length of 0.1 μm for intrinsic a-Si:H would decrease even further for extrinsic a-Si:H [5].

Therefore, the traditional p-n junction design, used for fabricating c-Si solar cells, is incompatible, for achieving higher efficiencies, with a-Si:H [5]. Since, this design relies heavily on carrier diffusion for charge collection. As a result, D. E. Carlson et al. (1976) introduced the p-i-n type concept for fabricating a-Si:H solar cell, which relies only on carrier drift as a means for charge collection [5]. Although, they reported a η of 2.4 %, by 1982, efficiencies as high as 10% were reported by other researchers [4, 5]. However, it was observed that the initial efficiency would subsequently decrease and stabilize at a lower efficiency value [5, 7, 8]. This phenomenon later came to be known as the Staebler – Wronski effect and is primarily caused by the photo induced degradation of the film [5, 7, 8].

Nevertheless, the Staebler – Wronski effect is less pronounced in a closely related phase to a-Si:H, which is the nc-Si:H phase. This phase was first deposited and reported by S. Veprek et al. (1968) via low temperature PECVD [5, 9]. Later on, after p and n-type a-Si:H were demonstrated, S. Usui and M. Kikuchi (1979) reported that nc-Si:H can be doped as well [4, 5]. Although, Hattori et al. (1987) used nc-Si:H as the doped layers of a p-i-n solar cell, it did not receive wide scale attention as an absorber layer [5]. This was because the nc-Si:H films at the time had high defect density and n-type nature [10, 11]. Nonetheless, this changed when U. Kroll et al. (1995) deposited intrinsic nc-Si:H using *very high frequency* (**vhf**)-PECVD [5]. He achieved this by reducing the oxygen content in the film through the use of gas purifier during fabrication [5]. Based on this finding, J. Meier et al. (1996) subsequently reported a fully nc-Si:H solar cell with an efficiency value of 7.7% [5, 10]. This greatly expanded research activity on nc-Si:H solar cells.

Subsequent studies by researchers on intrinsic nc-Si:H revealed that nc-Si:H absorber layers fabricated near the a-Si:H to nc-Si:H transition regime demonstrated higher solar cell η than highly crystalline nc-Si:H (far away from the transition regime) [2, 12]. This rise in the efficiency has been attributed to the microstructure of nc-Si:H near this regime [13]. Here the nanometer sized grains, instead of being closely packed into conglomerates, are dispersed in the amorphous matrix [13]. Thus the dangling bonds on the nanocrystal surface are efficiently passivated and the density of voids and cracks in the microstructure are minimized [13]. This is

unlike highly crystalline nc-Si:H, since it has high defect density resulting from voids, cracks, dangling bonds etc. within the micron sized conglomerates [13].

As a consequence, some of the unique electronic and optical properties of both the a-Si:H and pc-Si:H phases manifests itself to a certain extent in the nc-Si:H phase fabricated near the transition region. nc-Si:H solar cells, with absorber layers fabricated from this phase, have higher *Short-circuit Current Density* (**J_{sc}**) and stability compared to a-Si:H cells due to the presence of crystalline grains [13]. In addition, it has higher *Open-circuit Voltage* (**V_{oc}**) compared to the pc-Si:H cell due to the presence of the amorphous matrix in the microstructure [13]. Thus, this nc-Si:H phase has been the focus of thin film research for the past decade.

That said, over the years, various deposition methods were also investigated in order to deposit electronic quality thin film silicon [14]. However, rf-PECVD has become the industry standard due to its ability to continuously deposit uniform, high quality thin film silicon on large area substrates, and its integrability with roll-to-roll manufacturing process [14, 15]. Nevertheless, the primary disadvantage of fabricating thin films using rf-PECVD is its low deposition rate, which for device quality a/ nc-Si:H is around 1-2 Å/s [5, 11, 16].

This is a major economic stumbling block for thin film Si solar cell fabrication, since it implies long deposition times using conventional rf-PECVD, especially in the case of nc-Si:H, which requires absorber layer thicknesses over 1 µm [5]. As a result, one of the primary research priorities in thin film silicon solar cell is to increase the deposition rate up to 10-20 Å/s, while at the same time yielding equal if not better device quality films [5, 11]. If this is achieved then the cost of nc-Si:H solar cells can be reduced even further, thus making it even more competitive with the c-Si solar cells [5, 11, 17].

In trying to overcome this barrier, researchers have fabricated electronic quality thin film silicon at high deposition rates by modifying different parameters in the PECVD, such as *pressure*, *power*, *electrode distance*, *plasma frequency*, *gas flow rate* etc. [18]. Thus different processes have been named based on these parameter modifications, e.g. *high pressure (**hp**)-PECVD* [19, 20], *vhf-PECVD* [21] etc. But these parameter modifications introduced other

undesired ramifications. Such as, in the case of vhf-PECVD the deposited films have non-uniform thickness [21]. Although, this problem had been solved using ladder or U – type electrode [21], the industry is lethargic to such costly modifications when the improvement in material quality and deposition rate is not outright revolutionary.

Similarly, hp-PECVD suffers from dust formation which reduces the electronic quality of the film [6]. But, it has been shown from dusty plasma research by Ch Hollienstein et al. [22] that the negative silane radicals responsible for dust formation can be effectively removed from the plasma by turning it ON and OFF at certain frequencies and duty cycles [23]. This process is called *pulsed* (**p**)-PECVD and has been used by B. Rech et al. [2] and A. Madan et al. [24] to extensively study nc-Si:H for solar cell applications. But, they had reported mixed results for the deposition rate of nc-Si:H films and the characteristic parameters of the resultant nc-Si:H solar cells using p-PECVD compared to *continuous wave* (**cw**)-PECVD [2, 24, 25].

Consequently, in this study intrinsic nc-Si:H thin films and the resultant nc-Si:H solar cells were deposited on glass substrates at 150^{o}C substrate temperature using cw and p-PECVD. Working at this temperature would allow for the easy transfer of optimized recipes onto plastic substrates in the future. The objective was to investigate whether or not the structural and electronic properties of the intrinsic nc-Si:H films fabricated using p-PECVD improved compared to the cw-PECVD. Thereafter, the optimum film recipes, developed from both the processes, were used to fabricate nc-Si:H solar cells. The respective η and EQE of the cells were then characterized and compared.

The obtained results from this study will then be used as a preliminary step towards performing a comprehensive study on the influence of p-PECVD on the structural, electronic, and photonic properties of nc-Si:H. Eventually, the process, cw and p-PECVD, that yields better quality film would be used to fabricate nc-Si:H solar cells on plastic substrates.

To this end, this thesis was structured in a fairly chronological manner. The *Background* section was divided into three major segments. The first segment briefly overviewed the PECVD process and its parameters. In the second segment, the discussion gradually moved onto thin film

silicon microstructure, deposition physics, and its electronic properties. Thereafter, in the third segment, solar cell characteristic and loss parameters were covered. The information provided in the Background was by no means an exhaustive survey of the field. It was only a brief over view of the background information that would be used as a foundation when discussing the experimental results. The Background section was followed by the *Experimental Methodology* section, which aimed to concisely outline the experimental strategies undertaken to achieve the research objectives. This was followed by the *Results and Discussion* section. Lastly concluding remarks were made on what was achieved and possible future improvements.

Chapter 2: Theoretical Background

This chapter has been divided into three major sections. Although they are brief, each section successively aims to build on the information provided in the pervious section. The information provided here is short yet resourceful enough to setup precedence for explaining the observed experimental results in a concise and lucid manner. To this end, the three sections are: PECVD System, Materials Physics of Thin Film Silicon, and Thin Film Silicon Solar Cells.

2.1 Plasma Enhanced Chemical Vapor Deposition (PECVD) System

This section will begin by briefly highlighting the PECVD reactor schematic. Then it will describe the plasma structure, how it is formed, and the specific system parameters that govern the structural and electronic properties of the deposited film. Finally, powder formation in the PECVD process will be discussed followed by a brief description of p-PECVD.

2.1.1 Generic PECVD Reactor Schematic

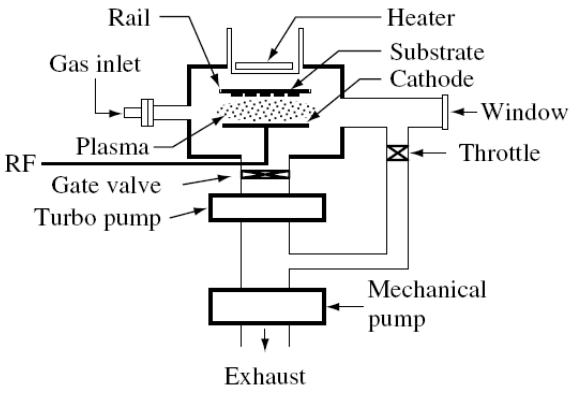

Figure 2.1: A simplified schematic of a PECVD system [11]. Image acquired from reference [11].

A generic PECVD (**Figure 2.1**) system consists of five core components:

1. A ***gas delivery system*** that controls the inflow and outflow of gases taking part in the deposition chamber [11]. It comprises of gas cylinders, pressure regulators, mass flow controllers and an assortment of gas valves [11].
2. A high vacuum ***deposition chamber***, where the PECVD reaction takes place. It houses a pair of capacitively coupled electrodes that are connected to the RF power feed through, a substrate holder for depositing the desired thin film, and a heater well [11].
3. A ***pumping system***, which maintains a specific user input pressure within the chamber. It is composed of high pressure gauges, a turbo-molecular pump and a mechanical rotary pump [7, 11].
4. A ***control panel*** that monitors and controls the chamber pressure, deposition chamber temperature, gas flow rate, and input power [7, 11].
5. And, an ***exhaust system*** that neutralizes reaction byproducts and un-reacted feed gases [7, 11].

After briefly over viewing the PECVD schematic the glow discharge structure will now be discussed.

2.1.2 Glow Discharge Structure

Macro-structurally the glow discharge volume can be broken down into three regions, which are:

1. The ***plasma***, which is a quasi-neutral mix of electrons, negative ions, negatively charged particles, and positive ions of silane and hydrogen related species [26].
2. And the ***Two Sheaths***, which are space charge regions located in between the plasma and the respective electrode, anode or cathode [26]. As the plasma begins to sustain itself through quasi electro-neutrality the potential drop that initially took place across the plasma between the two electrodes becomes constant while it drops rapidly near the electrode walls [26]. This sharp drop gives rise to a strong electric field that forces the small concentration of electrons present in the sheath to accelerate towards the plasma and positive ions towards the electrode walls [26]. It is these electrons that acquire enough energy to continuously ionize the gaseous reactants introduced into the plasma [26]. In addition, even though the plasma is quasi neutral the sheaths are mostly positive due to the low mobility of ions compared to the electrons [26].

(a) **(b)**

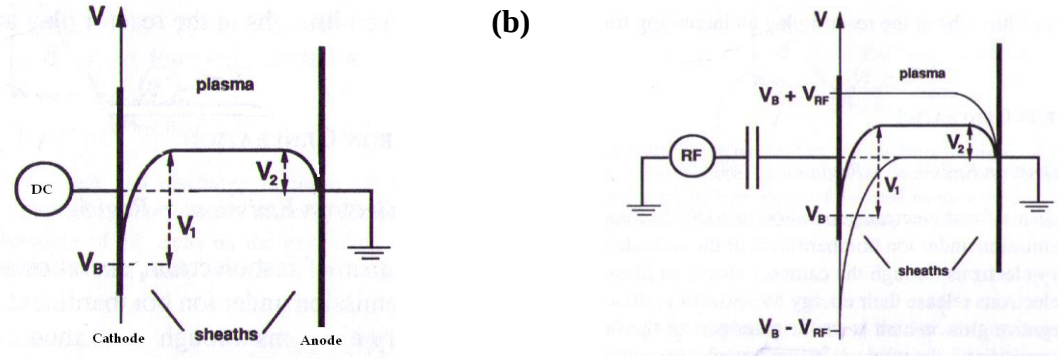

Figure 2.2: The potential distribution across the plasma and the two sheaths near the two electrodes for (a) DC bias, (b) RF (AC) bias [26]. Images acquired from reference [26].

Also, depending on the applied bias, DC or AC, across the electrodes, the potential distribution in the discharge would vary and as a consequence the plasma and the sheath structure would be different [26]. For DC bias the majority of the potential drop occurs near the cathodic sheath where as the potential drop near the anodic sheath is negligible (**Figure 2.2 a**)

[26]. However under applied AC bias, the sheath structure variation is quiet different from DC bias and can be classified under two categories based on the applied frequency regime:

1. ***Low frequency regime (below 1MHz):*** In this regime the discharge behaves like a DC discharge with alternating anodic and cathodic sheaths near the respective electrodes. This is because both the ions and electrons respond quickly to the change in the applied bias across the electrodes [26].
2. ***High frequency regime (ranges from 13.56 MHz, RF, to ~2.45 GHz):*** In this regime only the electrons are able to respond to the fluctuations in electrode bias, where as the ions due to their low mobility only observe the time averaged field [26]. As a consequence although the polarity of the respective electrodes alternate at a high frequency, the sheaths do not alternate (**Figure 2.2 b**) [26]. Furthermore as the frequency increases towards 100MHz, the wavelength of the applied frequency starts reaching the characteristic dimensions of the plasma volume [26]. This affects the potential distribution and consequently the electric field distribution across the plasma [26].

Having gone over the plasma macrostructure, the plasma formation physics will now be briefly discussed.

2.1.3 Plasma formation physics

The glow discharge mechanism is initiated, when a DC or an AC power input is applied across a pair of electrodes in a vacuum chamber where gaseous molecules, in this case silane (SiH_4; *notation form will be used only when molecules are discussed*) along with or without H_2 molecules are introduced [6]. The applied bias gives rise to a strong electric field, which causes some of the free electrons in the vicinity of the electrodes to accelerate under its influence. They then undergo many inelastic collisions with H_2 and SiH_4 molecules within the plasma. This excites these ground state molecules up to different higher electronic excited states depending on the amount of energy transferred during electron collision, which ranges from zero to several tens of electron volts (**Figure 2.3**) [14].

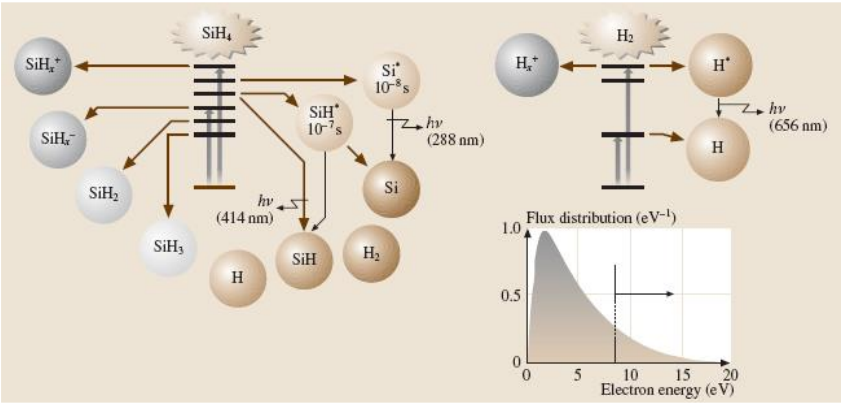

Figure 2.3: Schematic illustration of different species that result from the dissociation of SiH_4 and H_2 molecules after they are excited to their respective higher energy states [14]. The inset above demonstrates the normalized distribution of electron energy within the plasma [14]. Image acquired from reference [14].

At these excited energy states SiH_4 and H_2 molecule, dissociates into its ionic and neutral radical species, such as SiH_3, SiH_2, SiH, Si, and H respectively (**Figure 2.4**) [14]. These dissociation reactions are classified under primary reactions within the plasma [14]. The electrons lost, to the walls and the electrodes, are continuously replaced through the addition of new electrons from dissociated SiH_4 and H_2 molecules. This stabilizes the net concentration of electrons in the plasma.

$e + SiH_4 \rightarrow$	$SiH_4 + e$	$SiH_4 + H \rightarrow$	$SiH_3 + H_2$
	$SiH_2 + H_2 + e$	$SiH_4 + SiH_2 \rightarrow$	Si_2H_6
	$SiH_3 + H + e$	$SiH_3 + SiH_4 \rightarrow$	$SiH_4 + SiH_3$
	$SiH + H_2 + H + e$	$SiH_4 + Si_2H_6 \rightarrow$	Si_nH_m
	$SiH_2^+ + H_2 + e + e$		
	$SiH_3^+ + H + e + e$		
	$SiH_3^- + H$		
	$SiH_2^- + H_2$		
	Primary	**Secondary**	

Figure 2.4: Some of the primary and a few secondary reactions that occur during the plasma dissociation or glow discharge process [6]. Image acquired from reference [6].

Along with the generation of the desired *silane species* (**SiH_x**) within the plasma, such as SiH_3 - that act as the precursors for the thin film growth, many unwanted, low life time, reactive species, such as SiH etc., are also produced in the primary reactions [14]. However, these reactive species have low number densities. The respective number densities of such species are determined by working out the balance between their rate of generation and annihilation (**Figure 2.5**) [14].

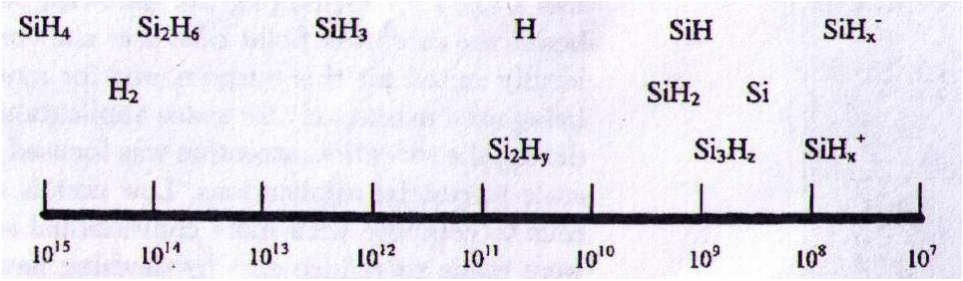

Figure 2.5: The approximate number density of different silane related species generated within rf-PECVD plasma [6]. Image acquired from reference [6].

Additionally, the densities of these reactive species may increase depending on the plasma parameter and the inflow rate of silane gases to the chamber [14]. For example, under high electric field, low pressure, and low silane dilution ratio, the reactant SiH_4 molecule is readily depleted within the plasma. As a consequence the reactive species formed within the plasma cannot react with other SiH_4 molecules or radicals [14]. Thus, during the deposition process, they are automatically incorporated in the film [14]. This leads to the fabrication of a poor quality film that structurally deteriorates quickly [14].

2.1.4 PECVD parameters

This section will briefly overview some of the deposition parameters that control the structural and electronic properties of a-Si:H and nc-Si:H thin film during PECVD processing.

i. Pressure: The potential required to sustain the plasma is a function of the pressure and electrode separation (discussed subsequently) [6]. At high pressures (> 1 Torr) the secondary reactions yielding *higher silane species* (**Si_mH_x**) will be favored along with the formation of

SiH_3, within the plasma bulk [6]. This will not only cause the formation of powder but will also increase the growth rate of the thin films significantly [6]. However, at even higher pressures (> 10Torr) the powder formation will be heavily favored over the thin film growth [6]. This is because the SiH_x cannot diffuse to the substrate in time to contribute towards film growth [6]. Thus they react with SiH_4 molecules and form longer chained Si_mH_x species which aids in the formation of powders [6]. It was reported that the optimum pressure for thin film deposition is *10-12 Torr* [18].

ii. Electrode gap: The distance between the electrodes also dictates whether the powder formation will be favored over thin film growth or not [6]. For longer electrode separation the SiH_3 will have to diffuse longer distances to reach the anode [6]. As a result the probability of powder formation greatly increases [6]. Besides, if the electrode distance is too small then the plasma becomes unstable. The optimum electrode spacing for thin film deposition is *1cm* [18].

iii. Substrate temperature: The temperature of the substrate surface plays an important role on the surface adatom mobility (e.g. SiH_3) [6]. This is because high temperature substrates provide larger amount of energy to SiH_x adatoms [6]. This in turn increases their adatom mobility [6]. With the extra mobility, the adatoms can now diffuse across the substrate surface and find an energetically favorable position (lowest free energy spot) [6]. One should also keep in mind that the application of even higher substrate temperatures results in the loss of hydrogen from the surface [6]. This causes the formation of large numbers of dangling bonds which increases the sticking coefficient of the surface and hence decreases the surface mobility of the adatoms [6]. Thus from research it has been shown that the optimum substrate temperature for thin film growth is in the range of 200^{o}C to 300^{o}C [6, 18].

iv. Power density: Increasing the power density to the plasma above 100 mW/cm^2 leads to the formation of higher polymeric radical byproducts within the silane plasma, which results in the formation of powder [6]. Furthermore, the high power density also introduces higher electric fields in the sheath layer [6]. This causes the positive ions to bombard on to the substrate surface [6]. Thus the dangling bond density in the deposited film increases [6]. Additionally the heavier polymeric silane species will bond to the substrate surface near the vicinity of the initial impact

position due to their low surface mobility [6]. As a result, the sum combination of the aforementioned effects leads to the formation of a porous film with poor electronic and structural properties [6]. It is observed from experimental results that the optimum power density value for films with good electronic properties ranges between 10 to100 mW/cm^2 [6].

v. Gas flow rate: The gas flow rate is also another important factor in the formation of good quality films [6]. A decrease in the gas flow rate increases the residence time of heavy and short lifetime radicals in the plasma [6]. This increases their contribution towards the thin film growth, which leads to a poor structural and electronic quality film [6]. In addition at higher flow rates the gas utilization rate is low [6]. As a consequence the flow rate should be optimized in order to obtain good quality films.

vi. Hydrogen dilution ratio: The addition of hydrogen gas with silane, during plasma dissociation, greatly improves the electronic property of the deposited a-Si:H thin film [6]. This is because, hydrogen acts to passivate the dangling bonds within the a-Si:H and the surfaces of the nanocrystalline grains in the nc-Si:H thin film. Additionally, excess hydrogen aids in structural growth [6]. Experimental studies have shown that the best a-Si:H and nc-Si:H material is achieved near the transition region between a-Si:H to nc-Si:H growth [6].

vii. Frequency: In solar cells industry almost all of the device quality films are produced at radio frequency (13.56 MHz) [6]. Nonetheless, this frequency can be increased to yield higher deposition rates [6]. However, at these high excitation frequencies, the wavelength becomes comparable to the substrate dimensions, which results in the formation of standing waves on the substrate surface [6]. These standing waves induce non-uniform deposition rate on the substrate surface, which leads to the deposition of thin films with non-uniform thickness.

The aforementioned deposition parameters have been briefly stated so that one comes to understand and appreciate the different experimental approaches taken in order to increase the growth rate of the thin film silicon. In the next section particulate formation will be further discussed.

2.1.5 Powder Formation

As mentioned in the previous section, the increase of power and pressure and the associated decrease in the electrode distance increases the deposition rate of the thin film silicon. However, under these conditions silicon particles ranging from nanometers to micrometers are also generated [22]. The presence of such small particles, modify the plasma by inducing changes in the electron density, electron temperature (energy), and plasma composition [22]. This primarily takes place when the particle number density increases high enough that the rate of electrons lost to the particles in the plasma is higher than that lost to the walls [22]. As a result the electron density in the plasma drops and the temperature of the remaining electrons rises [22]. This leads to the generation of larger quantities of reactive species, both ionic and neutral e.g. SiH_2, SiH etc due to the high energy collisions [22]. The incorporation of these species into the growing film increases the dangling bond density in the thin film microstructure, which significantly reduces the electronic quality of the film [22].

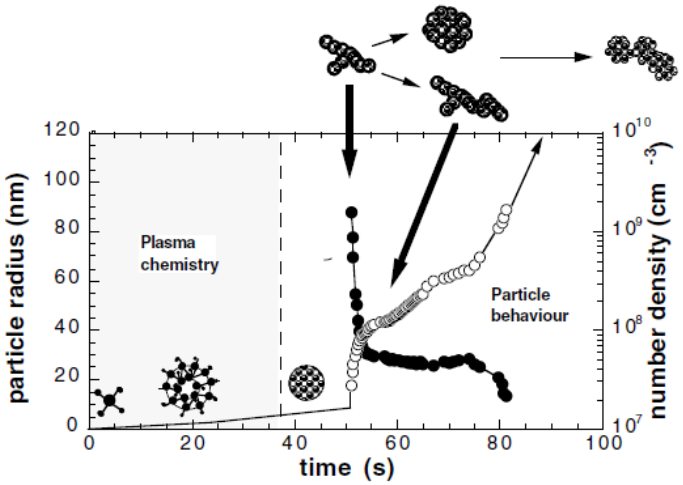

Figure 2.6: Particle radius (open circles) and number density (closed circles) as a function of time in a pure silane rf plasma [22]. Image acquired from reference [22].

Different models have been proposed in order to explain the growth of the micrometer sized silicon particles from the initial silane species in the plasma [22]. The most plausible model thus far, identifies the growth process of such particles in three major stages, namely *nucleation*, *agglomeration* or *coagulation*, and *accretion* (**Figure 2.6**) [22].

The nucleation stage is governed by the plasma chemistry and differs based on *homogeneous* and *heterogeneous* reactions [22]. But, only homogeneous reactions will be discussed in this brief overview since silane plasma reactions, even diluted, tend to transpire in such a manner [22]. For more information on the heterogeneous nucleation processes one may look up the research papers authored by Ch Hollenstein et al [22].

During ***nucleation***, the initial clustering of Silane species occurs through the polymerization of negative silane ionic species [22]. Negative silane species (after generation) are trapped in the plasma bulk by the sheath potential [22]. This allows them to undergo continuous polymerization reactions [22]. A possible polymerization pathway is shown in the following equation:

$$Si_nH_x^- + SiH_4 \longrightarrow \left(Si_{n+1}H_{x'}^-\right)^* + \left(H,\ H_2 \text{ products}\right) \qquad \textbf{(1)}$$

Where, a negative silane species/molecule ($Si_nH_x^-$) reacts with SiH_4 to form a Silane polymer. However, this newly formed silane polymer only becomes stable when it reaches the ground state by loosing excess energy. This occurs either by the redistribution of energy among the internal rovibrational modes or by a stabilizing collision with a third body before the auto-detachment lifetime [22]. Otherwise, the polymer disintegrates due to the excess energy acquired following the polymerization reaction [22].

The nucleation process continues until a critical number density of Si atoms is reached. Thereafter, nucleates of approximately equal number density of Si atoms start ***agglomerating*** or ***coagulating*** to form macro - particles up to a size range of 50 nm [22]. Upon reaching this size range, growth via agglomeration is replaced by the ***accretion*** of neutral or ionic monomers due to the charging of the particles, so as to maintain equilibrium with the plasma [22]. This process continues until the particle reaches micrometer size [22]. It has been observed that the dilution condition of the plasma affects the formation and the size of the particles, with much smaller sizes observed in diluted plasmas.

2.1.6 Pulsed (p)-PECVD

p-PECVD is capable of preventing the formation of particles in the plasma bulk and the incorporation of higher order and low life time silane species in the films at high deposition rate yielding conditions, such as high pressures and power and small electrode gap. This is possible, because the process modulates the plasma ON and OFF at different pulsing frequencies and duty cycles. During plasma ON time, a higher peak power is applied compared to the cw-PECVD, provided that the average powers are the same. This leads to the dissociation of a larger number density of Silane molecules and the subsequent generation of ionic, neutral, and Si_mH_x species compared to a cw-PECVD for the same time. Thereafter, during the plasma OFF time, the dissociated silane species, especially negative silane species that are precursors for nucleation, diffuse out. Concurrently, the deposition chamber is also replenished by the influx of SiH_4 molecules.

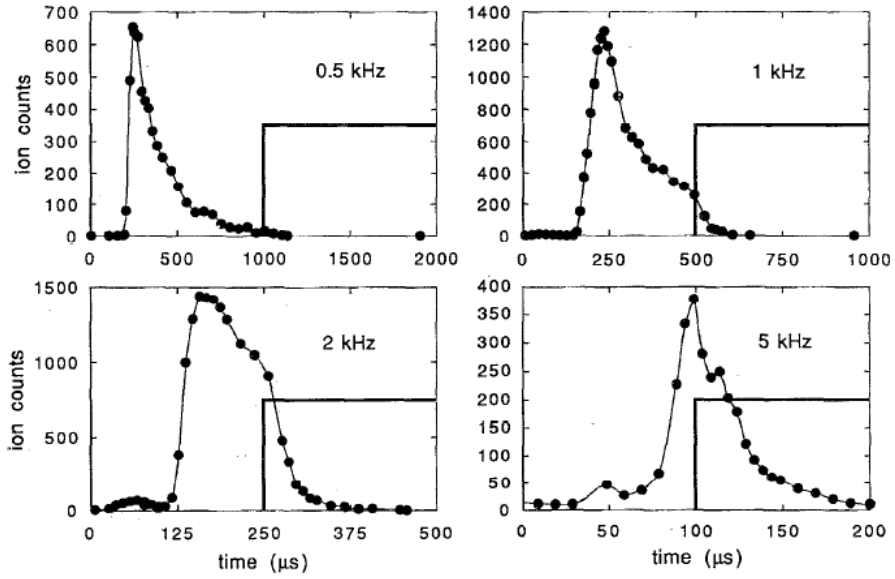

Figure 2.7: The $Si_2H_5^-$ intensity count for power modulation frequencies of 0.5, 1, 2, and 5 kHz respectively [23]. Images acquired from reference [23].

An example of the aforementioned discourse is illustrated in **Figure 2.7**. It shows the number counts of the $Si_2H_5^-$ species as a function of time [23]. The $Si_2H_5^-$ count drops during the plasma OFF time, because it is slowly emptied out of the discharge volume during the

afterglow period (plasma OFF time) [23]. However, as the modulation frequency increases, it is observed that fewer $Si_2H_5^-$ is able to leave the discharge volume up to the point where $Si_2H_5^-$ only accumulates in the plasma. This affects the resultant thin film quality (as discussed previously in *section 2.1.5*) [23].

Additionally, these conditions vary based on the plasma parameters, such as *pressure*, *power*, *frequency* etc. and the *modulation frequency* and *duty cycle*. This is because they increase or decrease the rate constants, hence lifetime, of the reactive species, which ultimately affects the resultant thin film quality. Thus the process needs to be optimized every time for different plasma conditions.

2.2 Thin Film Materials Physics

A brief overview of the structural and electronic properties of thin film silicon both a-Si:H and nc-Si:H will be provided in this section.

2.2.1 a-Si:H Thin Film

i. a-Si:H microstructure:

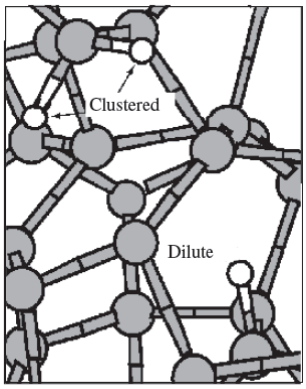

Figure 2.8: Computer animated model of the chemical bonding within a-Si:H [7]. The large gray spheres represent silicon, while small white spheres represent hydrogen atom [7]. The hydrogen atom can be found in dilute and clustered phases within the a-Si:H matrix [7]. Image acquired from reference [7].

The a-Si:H microstructure contains silicon atoms that have the same amount of bonding orbitals, four sp^3 orbitals, as that of c-Si [7]. However, it was observed that not all the orbitals bond with the nearest neighboring atoms, some of them are left dangling in the structure [7]. This helped to explain the lack of long range order, disarrayed structure, of a-Si:H (**Figure 2.8**) [7]. These unbounded orbitals, dangling bonds, impede the electrical conduction by trapping free electrons and holes in the thin film. This is the primary reason why a-Si:H demonstrates poor electronic properties. The reduction in the density of these dangling bonds is the key to achieving electronic quality a-Si:H. Researchers were able to overcome this barrier by diluting hydrogen into the silane plasma, which passivates the dangling bonds in the resultant film and hence improves their electronic quality [7, 11]. It is due to this hydrogen passivation that in device literature amorphous silicon is often referred to as hydrogenated amorphous silicon and vice versa [7, 11].

ii. a-Si:H thin film growth:

(a)

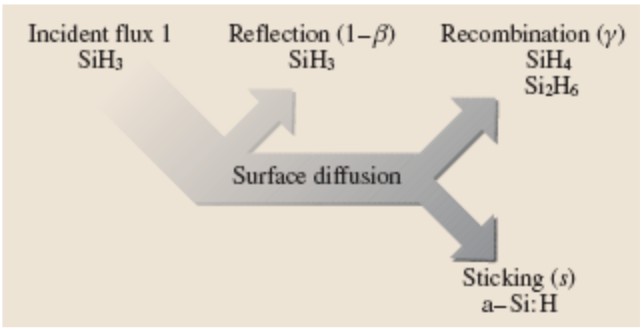

(b)

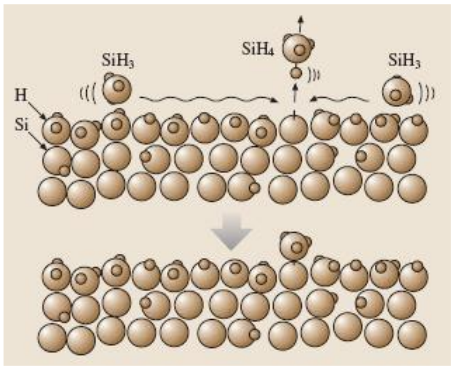

Figure 2.9: (a) A flow chart of the general surface reaction concept [14], **(b)** A visual representation of the surface growth of a-Si:H [14]. The small spheres in the diagram represent hydrogen while the larger spheres represent Si [14]. Images acquired from reference [14].

Experimental studies have shown that SiH_3 molecules are the primary precursors for thin film silicon growth [14]. However, out of the initial amount of SiH_3 molecules that are produced within the plasma and diffuse towards the film surface, only a certain fraction, β, is adsorbed onto the surface while the remaining fraction returns back to the plasma (**Figure 2.9 a**) [14]. Out of this remaining fraction, β, of SiH_3 molecules only a fraction, s, will bond with the underlying

surface [6, 14]. The remaining fraction, γ, will abstract hydrogen from the surface to form SiH_4 molecule or will undergo surface reaction with another SiH_3 adatom to form Si_mH_x, e.g. Si_2H_6 [14]. The byproducts of both these processes will leave the surface and diffuse into the plasma [14]. However, in the case of abstraction, a dangling bond is left behind on the film surface (**Figure 2.9 b**). Another SiH_3 adatom can attach itself to the film via this dangling bond or else it is covered up by the growing surface and thus retained in the bulk as a defect [14]. The bonding of SiH_3 adatom with the surface leads to a strong Si-Si bond, which aides in thin film growth [14].

iii. a-Si:H electronic properties:

Every semiconductor material has a *conduction band* (**CB**) and *valence band* (**VB**), and this is no different for amorphous silicon. But due to its amorphous nature it exhibits peculiar properties that are not demonstrated by its crystalline counterpart. The density of states, band tails, band edges, defects, and band gap states of a-Si:H are discussed below.

The ***Density of States*** (DOS) outlines the number of available states per unit volume an electron can occupy at certain energy [27, 28]. For c-Si the density of states abruptly ends at the CB and VB edges respectively [28]. This is attributed to the long range order of c-Si [31]. As a result the *band gap energy* (**E_g**), which is the difference between the *conduction band edge* (**E_c**) and *valence band edge* (**E_v**), is well defined. However for a-Si:H the abrupt endings of the density of states for the CB and VB at the respective band edges are replaced by broadened tails that extends well into the band gap region [31]. This is known as ***band tail***. This expansion of the density of states into the forbidden gap is related to the different bond lengths and angles arising from the lack of long range order within the a-Si:H matrix (**Figure 2.10**) [31].

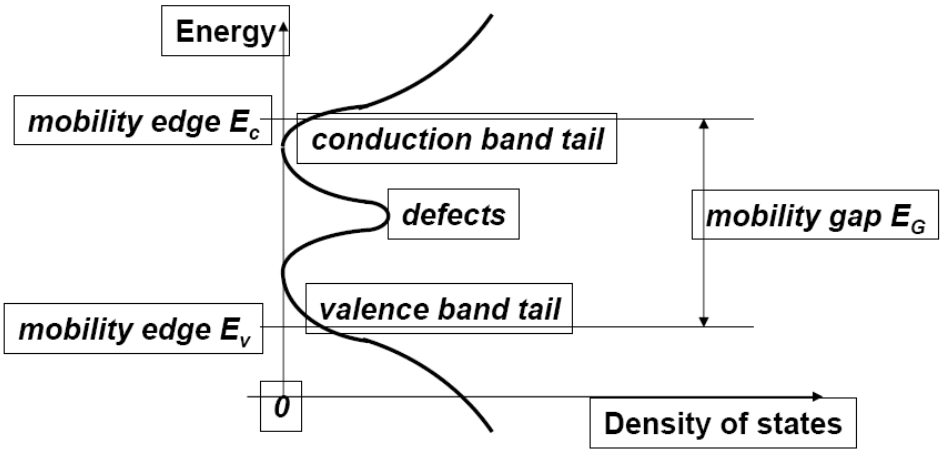

Figure 2.10: a-Si:H Density of States, g(E), distribution across the band gap (mobility gap) [3]. The steep band edges of c-Si are replaced by characteristic band tails that allow electron energy states in the forbidden gap [7]. The dangling bond induced defect states occupy the middle of the forbidden gap [7]. Image acquired from reference [3].

Although a-Si:H has exponential band tails, it has been shown from drift-mobility measurements that there still exists a well-defined band edge and by extension a E_g [7]. This ***band edge*** is defined as the energy that separates the extended states from the localized states. It is often termed the mobility edge due to the difference in the mobility above and below the edge. Above the edge the carrier transport is direct similar to c-Si, while below the edge the mobility is governed by hopping transport, which occurs due to carrier trapping and de-trapping [3]. The E_g of a-Si:H is around 1.7 – 2 eV [3]. It should be noted that there is no universal method to conclusively measure the band edges within the density of states. Nonetheless, internal photoemission measurements are often used to identify the E_g of a-Si:H [7]. Also, due to the extended VB tail compared to the CB tail, the hole mobility (μ_p) is couple of orders of magnitude smaller than the electron mobility (μ_n) in a-Si:H [3, 7].

Furthermore, a common feature of a-Si:H electronic band diagram is the existence of ***defect levels*** in between the VB and CB tails (**Figure 2.10**) [3, 7]. These defect DOS occur due to the presence of dangling bonds present within the amorphous matrix structure. Additionally, the absence of long range order allows a-Si:H to act like a direct band gap material. As a

consequence the selection rule for the conservation of momentum during electron excitation from VB to CB becomes irrelevant for a-Si:H compared to c-Si [6]. This enables a-Si:H to absorb light very efficiently compared to c-Si [6].

Doping is a frequent feature for any semiconductor. It is a process of introducing impurities into a system which perturbs the Fermi level (E_F) either in the direction of the CB or the VB. The dopants that donates an electron to the CB is called an n-type dopant. This moves the E_F closer to the E_c. Where as dopants that introduces holes in the VB is called a p-type dopant and as a result moves the E_F closer to the E_V. A semiconducting material that has a net doping concentration of either n or p-type dopants is called an n or p-type semiconductor.

Having said that, doping in a-Si:H is "digital" due to high density of band tail states and defects [3]. At low doping level the E_F is jammed by defects where as in high doping the E_F is situated in the band tail state [3]. This is because each electrically active dopant introduces a defect in the a-Si:H microstructure. Thus instead of the E_F moving into the bands for heavy doping conditions, similar to c-Si, it tends to move back towards the band gap center [3].

2.2.2 nc-Si:H Thin Film

i. nc-Si:H microstructure:

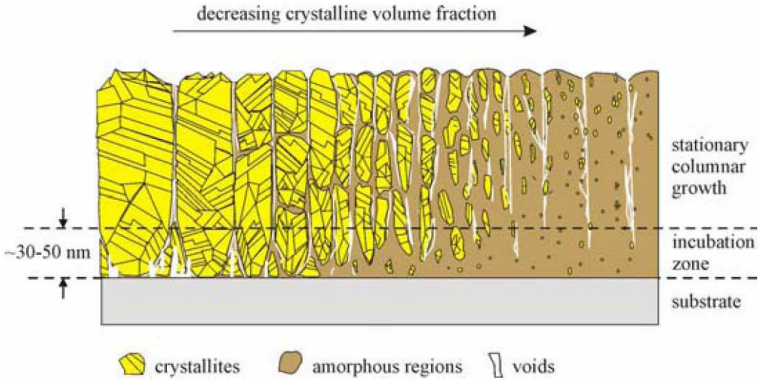

Figure 2.11: Pictorial representation of the crystalline and amorphous volume fractions as a function of the hydrogen dilution ratio [12]. For highly crystalline nc-Si:H films the nanocrystal grains are closely packed together to form micron sized conglomerates. Image acquired from reference [12].

The nc-Si:H microstructure is composed of nanometer sized grains closely packed together to form conglomerates that are embedded in an amorphous tissue (**Figure 2.11**). The sizes of these conglomerates vary between tens of nanometers to couple of microns. Additionally, voids and cracks are concurrently present within the nc-Si:H microstructure and becomes pronounced for highly crystalline nc-Si:H. Having said that, the crystalline volume fraction in the nc-Si:H is modulated by varying the hydrogen concentration in the silane plasma.

As the hydrogen dilution ratio in the plasma increases beyond the transition region, the crystalline volume fraction of the deposited film increases as well. This occurs due to the hydrogen etching of the growing thin film surface which aides in crystal growth (will be discussed later). Moreover, the structural nature of the nc-Si:H at the onset of thin film growth, is not crystalline at all, rather it is amorphous. This initial thickness, which spans tens of nanometers, is called the ***incubation layer*** and it results from the impeded grain growth rather than the suppressed nucleation of nanocrystals [13]. This layer thickness decreases with increasing hydrogen dilution ratio.

ii. nc-Si:H thin film growth:

Unlike a-Si:H, where SiH_3 plays the sole basic building block for thin film growth, nc-Si:H thin films require the contribution of both SiH_3 precursor and atomic hydrogen [14]. Having said that, three different growth models have been proposed in order to explain the growth of nc-Si:H [14]. They are briefly discussed below:

a. The surface diffusion model

The surface diffusion model was proposed in order to explain the observed rise crystallinity in thin film silicon for large hydrogen dilution ratio within the plasma [14]. The model concludes *two primary roles* of hydrogen for this phenomenon [14]. The *first* being the uniform surface coverage with strong Si – H bond and the *second* being the localized heat generated from the hydrogen exchange reactions (**Figure 2.12**) [14].

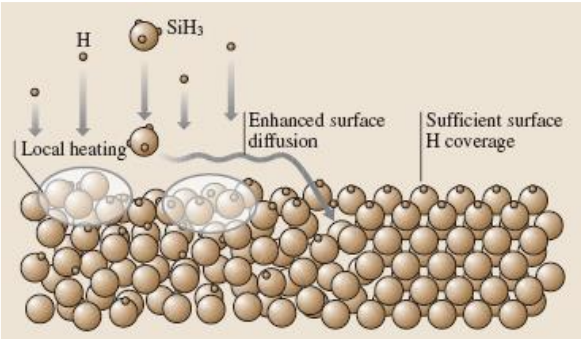

Figure 2.12: nc-Si:H growth using the surface diffusion model [14]. Image acquired from reference [14].

The sum combination of both these effects, forces the SiH_3 adatom to diffuse longer distances across the surface in order to locate an energetically favorable site [14]. The successive iterations of this process lead to the formation of a nucleate which ultimately grows and develops into a nanocrystalline grain [14]. However, the diffusion model failed to explain the decrease in film deposition rate with increasing hydrogen dilution ratio within the plasma [14].

b. The etching model

The etching model was proposed in order to explain the decrease in the deposition rate with increasing hydrogen dilution ratio. The model stated that the incident atomic hydrogen breaks the weak Si-Si bonds on the growth surface. The detached Si atoms and SiH_x then react with hydrogen atoms on the film surface to form SiH_4 molecules that diffuse back into the plasma while leaving behind dangling bonds on the surface (**Figure 2.13**) [14].

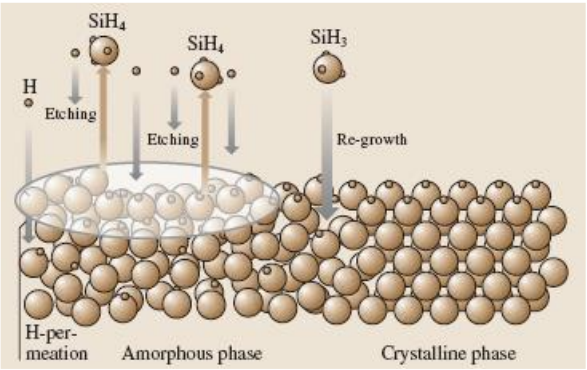

Figure 2.13: nc-Si:H growth using the etching model [14]. Image acquired from reference [14].

These vacant sites are then taken up by SiH_3 adatoms which form strong Si-Si bonds. The continuous iteration of the aforementioned process leads to the formation of a long range ordered structure [14]. As the hydrogen dilution ratio in the plasma increases the etching rate on the growth surface becomes more pronounced as well [14]. Although this increases the density of strong Si-Si bonds, which leads to an increase in crystallinity of the film, it also decreases the deposition rate of nc-Si:H.

c. The chemical annealing model

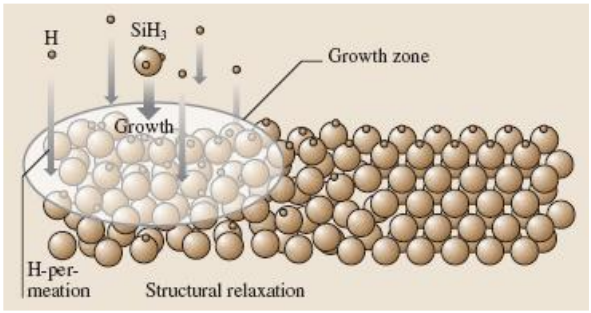

Figure 2.14: nc-Si:H growth using the chemical annealing model [14]. Image acquired from reference [14].

The chemical annealing model was proposed to explain the transformation of a-Si:H monolayers, deposited alternatively between hydrogen plasma treatments, to nc-Si:H phase without any significant reduction in the thickness of the film, as expounded by the etching model (**Figure 2.14**) [14]. The model states that the atomic hydrogen from the plasma permeates through the growth zone (film subsurface) and reacts with Si – H or strained Si – Si bonds [13]. The exothermic reactions rearrange the silicon network and enhance the crystal nucleation within the growth zone. This leads to the formation of crystalline regions without any significant removal of Si atoms from the thin film matrix [13, 14]. The rearrangement of the silicon network through the structural relaxation is also speculated to raise free volumes within the network [14]. This also serves to explain the presence of crack – like and spherical voids within the nc-Si:H bulk [14].

After briefly over viewing the *surface diffusion, etching,* and *chemical annealing model*, the nc-Si:H electronic properties will now be discussed.

iii. nc-Si:H electronic properties:

The density of states of the nc-Si:H are similar to that of a-Si:H. They both have band tail states to go along with their bulk density of states. However, the band tail state energy widths are much smaller in nc-Si:H than in a-Si:H [29]. This results from the crystalline volume fraction in nc-Si:H which is inversely proportional to the band tail energy width [29]. Thus as the crystallinity of the material increases with increasing hydrogen dilution ratio, the band tail energy width of the nc-Si:H concurrently decreases. Additionally, this crystalline volume fraction also improves the carrier mobilities in nc-Si:H compared to a-Si:H (**Table 2.1**).

Table 2.1: Mobility values for a-Si:H and nc-Si:H

Material	**Electron Mobility ($cm^2V^{-1}s^{-1}$)**	**Hole Mobility ($cm^2V^{-1}s^{-1}$)**
a-Si:H	~1	~0.001
nc-Si:H	~1-100	1-2 [17, 18]

Furthermore, the *photoconductivity* ($\boldsymbol{\sigma_{ph}}$) and σ_D are related to the carrier mobilities via the following equations:

$$\sigma_{ph} = e(\mu_p + \mu_n)G\tau \quad \textbf{(2)}$$

$$\sigma_D = e(p_o\mu_p + n_o\mu_n) \quad \textbf{(3)}$$

Where, $\boldsymbol{p_o}$, $\boldsymbol{n_o}$, $\mathbf{G}$, $\boldsymbol{\tau}$ represents, equilibrium free *hole concentration*, *equilibrium free electron concentration*, *electron-hole pair generation rate*, and *carrier life time* respectively [8]. Hence, the σ_{ph} and σ_D of the nc-Si:H are higher than that of a-Si:H (**Figure 2.15**) and rises with increasing crystallinity [12].

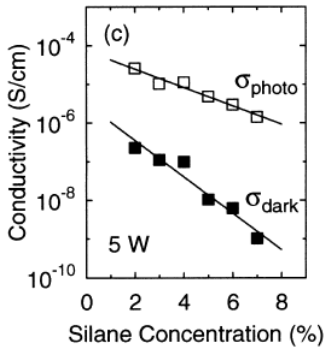

Figure 2.15: σ_{ph} (open square) and σ_D (closed square) conductivity of intrinsic thin film silicon with decreasing silane concentration [12]. Image acquired from reference [12].

The shallower rise in σ_{ph} curve in comparison to the σ_D curve with decreasing silane dilution ratio is associated with τ and G. Although τ increases with increasing crystallinity of the material, it is offset by the rise in the voids and cracks in the nc-Si:H microstructure. This net effect leads to a steady decrease in τ with increasing crystallinity of the nc-Si:H. Moreover, G is directly proportional to the *absorption coefficient* (**α**) of the nc-Si:H [8]. Thus, as the α decreases (for certain range of photon energies) with increasing nc-Si:H crystallinity, G decreases as well. Having said that, in general for device quality intrinsic nc-Si:H, the σ_{ph} and σ_D are on the order of 1E-6 – 1E-4 S/cm and 1E-8 – 1E-6 S/cm respectively [12, 31].

The nc-Si:H thin films can be doped p-type or n-type through the addition of tri-methyl boride or phosphine, which incorporates boron or phosphorous impurity atoms in the thin film microstructure respectively. In such a scenario the σ_{ph} and σ_D of the respective p-type and n-type materials rises up to the range of 1E0 – 1E1 S/cm [32]. The near parity between σ_{ph} and σ_D is due to the rise in defect density which significantly drops the *minority carrier life time* ($\boldsymbol{\tau_{minority}}$) [8]. In addition, impurities such as Oxygen, Nitrogen, and Carbon, in excess concentration of 1E19 cm^{-3}, have been known to make the intrinsic films n-type. This increases the σ_D of the nc-Si:H significantly, albeit in the range of 1E-3 – 1E-4 S/cm [10, 33].

The impurities, apart from segregating to the grain boundaries, has been linked with the decrease of the nanocrystal grain size in nc-Si:H [33]. Additionally, similar to intentional

dopants, impurities also introduce defects into the thin film, which reduces the long wavelength (λ) spectral response of the cell [34]. This reduces the J_{sc} of the cell respectively [34].

2.3 Thin Film Silicon Solar Cells

This final section will briefly discuss the p-i-n solar cell device structure, solar cell efficiency characteristics, and the quantum efficiency (QE) of the solar cell.

2.3.1 p-i-n junction solar cell device structure

Thin film silicon solar cells, both a-Si:H and nc-Si:H, are fabricated in a p-i-n device structure. This structure is ***drift based***. On the other hand the traditional c-Si based cells have a p-n device structure, which is ***diffusion based***. The preference of the p-i-n structure over the p-n structure is due to the high defect density in thin film silicon compared to c-Si. Furthermore, this defect density becomes more pronounced for doped compared to undoped thin films. As a result, the already low diffusion length of ~0.1 μm for undoped thin film silicon decreases even further for doped films [5]. This is highly inefficient for a p-n based design, since it relies on minority carriers to diffuse to the majority carrier regime. Consequently, most of the photocarriers will be lost through bulk recombination, before extraction, due to the high defect density in the film. Thus, in order to avert carrier losses and increase the η of the cells, a drift based structure is used. The schematic outline of the p-i-n solar cell used in this study is shown in **Figure 2.16**.

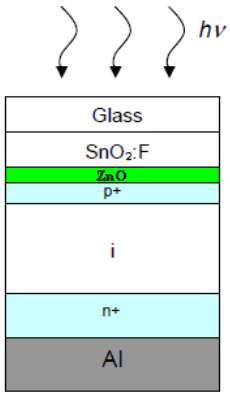

Figure 2.16: Outline of the p-i-n solar cell structure used in this work [31]. The cell is designed so that the majority of the photo-generation occurs in the i – layer [31]. The ZnO and SnO_2 are the Transparent Conductive Oxide (TCO) top contact whereas the Al is the back contact of the solar cell [31]. Image adapted from reference [31].

The thin film solar cells are designed so that the doped layers (p and n) are as thin as possible and the absorber layer (i – layer; *used interchangeably*) is as thick as possible. This is because the overwhelming majority of carriers generated in the doped layers are lost due to recombination. Furthermore, in order to sweep the photo generated carriers to its respective majority carrier regions a built in electric field is generated in the i – layer. This is achieved by heavy doping both the doped layers. As a result the p – i and i – n junctions extend deep into the absorber layer. In addition, the absorber layer thickness is tuned so that the depletion regions from both these junctions (p – i and i – n) meet. This results in the complete depletion of the i – layer. In such a scenario the entire band of the i – layer tilts and the photo-carriers generated in the i – layer, having higher mobility due to lower defects, are easily swept to their majority carrier regions due to the built in electric field.

2.3.2 p-i-n Solar Cell Device Configuration

Due to the versatility of PECVD deposition technique, which is capable of depositing on a variety of substrates such as plastic, glass, statinless steel etc., two different designs are concurrently employed for fabricating thin film solar cells. They are *substrate* and *superstrate configurations* respectively. The difference between the two is that, in the ***substrate***

configuration the light enters the cell through the opposite end of the substrate side (**Figure 2.17 a**). This is used mainly for opaque substrates e.g. stainless steel. Whereas in the ***superstrate configuration*** the light enters the cell from the substrate side (**Figure 2.17 b**). This is mostly used for transparent substrates e.g. glass and plastic.

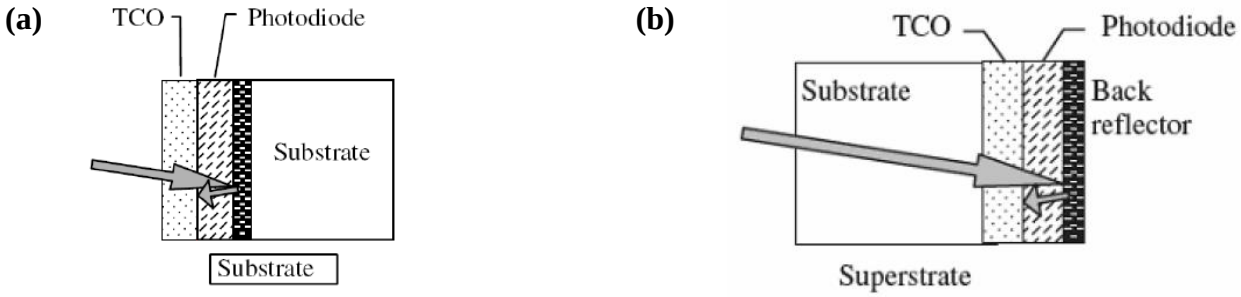

Figure 2.17: An outline of the thin film solar cell in **(a)** substrate configuration and **(b)** superstrate configuration respectively [7]. Images acquired from reference [7].

Also, for both the design configurations the p – layer is used as the ***window layer***, i.e. the layer that faces the incident light. This is because the majority of the incident photon absorption (hence electron hole pair, EHP, generation) occurs near the absorber layer and the window layer interface. However, the hole mobility is very low compared to the electron mobility in both the a-Si:H and nc-Si:H (**Table 2.1**) [6, 7]. Thus in order to prevent the loss of holes due to recombination, the p – layer is placed first in the direction of the incident light [6]. As a result the holes, on average, need to travel a short distance [6].

2.3.3 Solar cell efficiency parameters/characteristics and loss mechanism

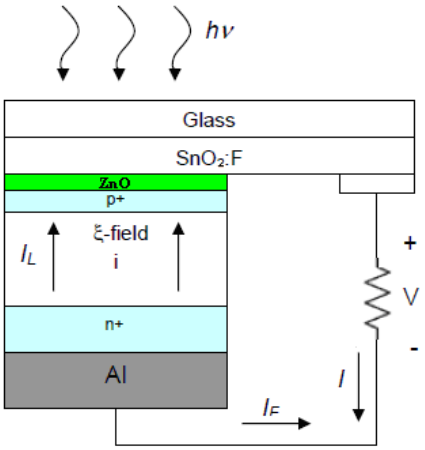

Figure 2.18: p-i-n thin film solar cell connected to a resistor load [31]. Image adapted from reference [31].

Figure 2.18 shows a schematic diagram of a p-i-n solar cell connected to a resistor. The flux of incident photons in the solar cell generates photoexcited carriers in the absorber layer. These carriers are then swept to their respective majority carrier regions by the built in electric field. This generates a *photoexcited current* (**I_L**) in the reverse bias direction of the solar cell [31]. The I_L then causes a voltage drop across the resistor, which in turn forward biases the solar cell, with a *forward biasing current* (**I_F**) [31]. As a result the produced net current, in the reverse biasing direction, is expressed along with the ideal diode equation as follows:

$$I = I_L - I_F = I_L - I_o\left(e^{\frac{qV}{kT}} - 1\right) \qquad \textbf{(4)}$$

Although this is an over generalization, nonetheless the key ideas can be briefly overviewed from the aforementioned equation. Two extreme cases are of particular interest. They are the V_{oc} and J_{sc} (**Figure 2.19**). The $\boldsymbol{V_{oc}}$ is achieved when the resistor resistance, R, approaches infinity. This reduces the net current density (J) to zero. On the other hand the $\boldsymbol{J_{sc}}$ is attained when resistance of the resistor reaches zero, implying that the voltage drop (V) across the resistor will

be zero [31]. J_{sc} and V_{oc} are the maximum theoretical parameters achieved by the respective device.

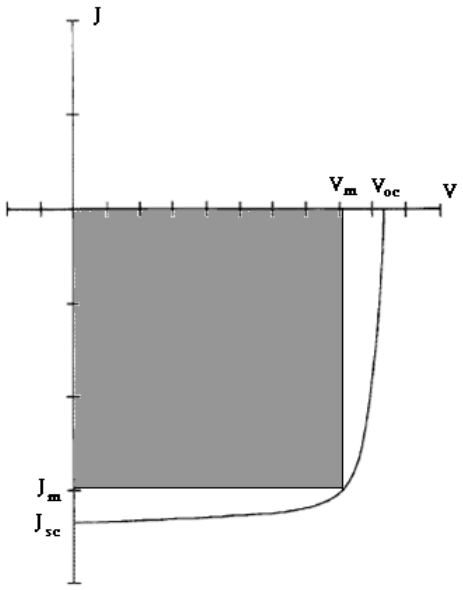

Figure 2.19: A sketch of the J-V curve of a solar cell, where J, V, J_{sc}, V_{oc}, J_m, and V_m are the *current density*, *applied bias*, *short – circuit current density*, *open – circuit voltage*, *current density at maximum power point*, and *the applied bias at maximum power point* respectively.

Although the J_{sc} and V_{oc} are the maximum J and V of the solar cell, operating the cells at these limits do not generate any power [35]. The maximum power from the solar cell is obtained from the *maximum power point*, $\mathbf{P_m}=J_m x V_m$ (it is the shaded area in **Figure 2.19**). The un-shaded areas are the lost power and to reduce these areas the cells are designed so that the J-V curve is as square as possible. The parameter for determining the "squareness" of the cell is called the ***Fill Factor*** (**FF**). It is the ratio of the P_m with the product of J_{sc} and V_{oc} and is expressed as follows:

$$FF = \frac{J_m V_m}{J_{sc} V_{oc}} \qquad \textbf{(5)}$$

Also, the $\boldsymbol{\eta}$ of the cell is determined by the ratio of the P_m to incident *Light Power Density* ($\mathbf{P_s}$). It is expressed through the following equation:

$$\eta = \frac{J_m V_m}{P_s} = \frac{J_{sc} V_{oc} FF}{P_s} \quad \textbf{(6)}$$

Having said that, the V_{oc} is governed by the following factors:

1. Interface effects, especially the p/i interface [36]
2. Activation Energy (E_A) of the doped layers

Poor p/i interface and high E_A of the p – layer decreases the V_{oc} of nc-Si:H solar cells. Additionally, the J_{sc} depends on the following factors:

1. Thickness of the absorber layer [36]
2. Light trapping [36]
3. Impurity concentration and Defect density in the absorber layer

The thickness of the absorber layer for nc-Si:H solar cells should be in the range of 1 to 2 μm. A thicker absorber layer is required for nc-Si:H, compared to a-Si:H, since it has a lower α (for certain photon energies) than the latter. Additionally, adequate structures should be set up so that the maximum intensity of the incident light is transmitted into the cell and is trapped for absorption. This includes the use of highly transparent TCO layer for a wide range of λ, highly crystalline p – layer for reduced absorption of shorter λ, and advanced light management structures near the back electrode which will scatter the incident light back into the absorber layer. Ideally, the light management structure, near the back electrode, is designed in such a way that the scattered light will have a higher critical angle at the front contact TCO layer. As a result the light will be internally reflected within the cell until it is absorbed. If the aforementioned factors are properly managed then the full potential of solar cell material can be efficiently utilized [36].

Aside from the efficiency parameters, the two primary sources of power losses in solar cells are ***Series resistance*** (**R_s**) and ***Shunt resistance*** (**R_{sh}**). Ideally for solar cell applications, the R_s

should approach zero and R_{sh} should approach infinity. An increase in R_s has three primary causes, they are:

1. Impedance of the current through the p-i-n layer
2. High contact resistance between metal/TCO contact and silicon, and
3. The resistances of the metal and TCO contacts themselves [35]

A decrease in the R_{sh} occurs when there is an alternate path for light generated current, which reduces the overall current flowing through the cell. This leads to a decrease in the V_{oc} of the cell as well. A low R_{sh} may be caused by the following:

1. The inadequate electrical isolation of the individual cells
2. Manufacturing defects, such as contact between the n – layer and the p – layer without the i – layer in between

A rise in R_s and a drop in R_{sh} not only affects the FF for the worse, but a pronounced affect significantly decrease the J_{sc} and V_{oc} respectively [35]. An approximate value of the R_s and R_{sh} can be found by taking the slope of the J-V curve at the V_{oc} and J_{sc} point respectively [35].

2.3.4 Quantum Efficiency (QE)

QE of the solar cell is defined as the ratio of the collected photogenerated carriers to the number of incident photons of a certain λ on to the solar cell [35]. More aptly put, it is the collection probability due to the generation profile of a certain λ, integrated over the entire device thickness and normalized by the incident photon flux at that λ [35].

The QE of the cell is expressed through the following formula:

$$QE = \eta_{col}(\lambda) = \frac{i_{ph}(\lambda)}{e\phi_{ph}(\lambda)} \quad \textbf{(7)}$$

Where, $\boldsymbol{i_{ph}}$ is the photocurrent, $\boldsymbol{e}$ is the charge of the electron, $\phi_{ph}(\lambda)$ is the number of incident photons of a certain λ per unit area per second *or* the incident photon flux at a specific λ [31].

There are two types of QE measurements: ***external quantum efficiency*** (EQE) and ***internal quantum efficiency*** (IQE) [35]. In the EQE all the photons of a certain λ incident on the device are taken into account, whereas in the IQE only the transmitted photons of a certain λ are used [35]. Thus the $\phi_{ph}(\lambda)$ will be different between EQE and IQE (**Equation 7**). Moreover, the IQE depicts the true potential of the cell, had the top surface not reflected a portion of the incident photons.

In general, the IQE is calculated by modifying the EQE with the reflection and transmission measurements from the solar cell device [35]. Nevertheless, in most cases the EQE of the cell is quoted. The EQE reveals important information about the absorption losses in the cell [31, 35]. For example, Low EQE at shorter λ (higher energy photons) may indicate losses in the electrical contacts, poor p-i interface etc., also losses at medium λ are related to bulk recombination losses, and lastly losses at long λ (low energy photons) are related to poor light management, thinner absorber layer, larger band gap of the thin film etc. [35].

Chapter 3: Experimental Design

The scope of this research was to investigate whether the structural and electronic properties of the nc-Si:H solar cell absorber layer improved with the use of p-PECVD instead of cw-PECVD. In order to fulfill this objective, the experiments were essentially divided into the following two major segments:

1. Intrinsic nc-Si:H thin film deposition and characterization
2. nc-Si:H solar cell design, fabrication and characterization

Segment 1 was further subdivided into two research phases. In the *first phase*, emphasis was placed on optimizing the material quality vis-à-vis structural and electronic properties under certain deposition conditions using cw-PECVD. Thereafter, in the *second phase*, this optimum recipe was further subjected to p-PECVD and similar characterization techniques applied in the first phase were reapplied in order to identify the best recipe. Subsequently, in *Segment 2*, the optimum recipes from both these processes, cw and p-PECVD, were used to fabricate the absorber layers of the thin film solar cell devices. These respective research segments and the specific deposition and characterization tools and techniques employed to achieve the desired objective will be discussed in this section.

3.1 Intrinsic nano-crystalline silicon (nc-Si:H) thin film

3.1.1 Phase 1: Depositing intrinsic nc-Si:H thin film via cw-PECVD

The nc-Si:H thin films were deposited on 3 inch diameter Eagle 2000 glass wafers in the *Reel to Reel* (**R-to-R**) Deposition system.

Figure 3.1: A rough outline of the Reel to Reel (R-to-R) deposition system used in this research. It consists of a Load Lock (LL), PECVD, and ZnO/ITO sputter chamber. The substrate is mounted into and out of the system through the LL.

It is a specially designed 3-chamber system, comprising of a PECVD, Load Lock (LL), and ZnO/ITO Sputter chamber respectively (**Figure 3.1**), in which the substrate career, housing the thin film substrate, is transported from one chamber of the system to the other without requiring the user to break the vacuum [37]. The key advantage of this system is its ability to deposit films on plastic rolls. This allows the user to optimize film recipes on glass substrates and then transfer the recipe onto a plastic substrate seamlessly without the need for a new deposition system, which would otherwise require the modification of the thin film deposition conditions.

During the thin film optimization process all of the deposition parameters were fixed at specific set points except for hydrogen flow rate. Thus *Power*, *Deposition pressure*, *Substrate temperature*, and *Silane flow rate* were fixed at certain values due to system constraints, while the *Excitation frequency* and *Electrode gap* were pre – fixed by the manufacturer and were not changed in order to avoid over complications. Since, the aforementioned PECVD parameters

were not optimized the results reflected in this report are by no means the optimized parameter values on the R-to-R system. The set and pre-fixed system parameters are discussed below:

i. Set parameters:

1. ***Deposition pressure:*** was fixed close to the maximum allowable limit in the PECVD chamber, namely 1000 ± 2 mTorr. Although, it has been reported that the pressures in the range of 10 Torr yields optimum quality films, for this experiment such working pressures were not employed due to time constraints [18].
2. ***Applied power:*** was set at 5 ± 0.05 W. It was intentionally kept low in order to reduce the affect of ion bombardment on to the film surface at low deposition pressures. Heavy ion bombardment on to the growing surface has been reported to reduce the crystallinity of the nc-Si:H film [14]. The low power also resulted in a lower deposition rate. Nonetheless, since two processes (cw and p-PECVD) are being compared the relative results between them were of primary research interest.
3. ***Substrate temperature:*** was kept at 150^{o}C by setting the heater well and the graphite heater temperatures of the PECVD system at 250 ± 20 ^{o}C and 250 ± 10 ^{o}C respectively. The optimum temperature (200^{o}C) for obtaining high quality nc-Si:H was not used, since this work is a precursor work for depositing nc-Si:H onto plastic substrates, which have low temperature tolerance limit [18].
4. ***Silane flow rate:*** was fixed at 2 sccm. The decision to fix the silane flow rate while varying the hydrogen flow rate was primarily rooted in the desire to abstain from producing excessive dust particles in the system.

ii. Pre-fixed parameters:

1. ***Excitation frequency****:* was preset by the manufacturer at 13.56 MHz and is the industrial standard for depositing thin film silicon using PECVD. Thus the excitation frequency was not changed.
2. ***Electrode gap:*** was prefixed by the manufacturer at 1.93 ± 0.06 cm. This electrode gap was not altered due to research time constraints, even though high quality nc-Si:H films were achieved for 1 cm electrode spacing at high pressures [18].

Upon setting the PECVD deposition parameters at the aforementioned values, a set of films were deposited at different hydrogen dilution ratios for two hours in order to identify the transition region from a-Si:H and nc-Si:H (**Table 3.1** and **Appendix: Phase 1**). This is because, improved device quality nc-Si:H films have been observed near the transition region. Additionally, the deposition rates of the films at each hydrogen dilution ratios were concurrently determined.

Table 3.1: Thin film silicon *phase* and the *deposition rate* (Å/s) for different hydrogen dilution ratios ranging from 98% to 99.01 %. The thin film deposition time was two hours.

Sample	**[H_2] flow rate (sccm), with [SiH_4] flow rate of 2 sccm**	**Hydrogen Dilution Ratio** $\left(\frac{[H_2]}{[H_2]+[SiH_4]}\right)$	**Sample Phase**	**Deposition Rate (Å/s)**
Sam007 (a & b)	98.0 + 3	98.00%	Amorphous	0.303 + 0.004
Sam012 (a & b)	112.5 + 3	98.25%	Crystalline	0.277 + 0.004
Sam008 (a & b)	125.0 + 3	98.43%	Crystalline	0.252 + 0.006
Sam013 (a & b)	137.5 + 3	98.57%	Crystalline	0.234 + 0.004
Sam009 (a & b)	150.0 + 3	98.68%	Crystalline	0.22 + 0.004
Sam010 (a & b)	175.0 + 3	98.87%	Crystalline	0.194 + 0.001
Sam011 (a & b)	200.0 + 3	99.01%	Crystalline	0.16 + 0.003

In order to calculate the deposition rates of the films, photoresist was applied at selective regions on the film surface. Then the film was etched in TRION RIE and the photoresist was subsequently removed using Acetone. Thereafter the thickness of the etched film was measured across the edge using DEKTEK 8 STYLUS PROFILER. Finally, the deposition rates of the films were calculated by taking the ratio of the thickness and deposition time (2hrs).

From the initial survey it was observed that the transition region, for the specified set of parameters, occurred between 98 – 112.5 sccm (98 % – 98.25 %) hydrogen flow rate. Also, it was noted that the Deposition rate had an inverse relationship with hydrogen dilution ratio. The highest deposition rate of 0.303 + 0.004 Å/s was achieved for 98% and the lowest deposition rate of 0.16 + 0.003 Å/s was achieved for 99.01% hydrogen dilution ratios respectively.

Using the information gained from the initial survey, same hydrogen dilution ratios were used to deposit 300nm thick films. This allowed for an adequate comparison of the structural and

electronic properties of nc-Si:H thin films at different hydrogen dilution ratios. For each deposition run, films were deposited on two separate substrates simultaneously. The film deposited on one of the substrates was used for characterizing the structural properties. This was measured by observing the crystallinity and the crystal orientation using Raman Backscattering and XRD spectroscopy respectively. While the film deposited on the other substrate was used for measuring the σ_{ph} and σ_D and photoresponsivity of the nc-Si:H films.

3.1.2 Phase 1: Characterizing intrinsic nc-Si:H thin film deposited via cw-PECVD

i. Raman backscattering spectroscopy measurement:

As mentioned previously, there are two primary phases in nc-Si:H, amorphous and crystalline phase respectively [4]. In the amorphous phase there exists lot of dangling and strained bonds due to the lack of long range order, whereas the crystalline phase has long range order. As a result of this difference in the bonding structure of the atoms, the Raman backscattered photons have different frequency shifts. This translates into different spectroscopic data for the amorphous and crystalline phase respectively. Thus the backscattered photons from the pure amorphous phase shows a broad Gaussian like Raman spectra centered at 480 cm^{-1} *Transverse Optical* (**TO**) whereas the backscattered photons from the crystalline silicon phases has a sharp peak at 520 cm^{-1} TO [37]. This disparity is then exploited in order to qualitatively determine the crystalline and amorphous volume fraction present within nc-Si:H.

The Raman Spectra for the deposited silicon thin films were acquired using Renishaw Micro-Raman 1000 spectrometer with a 488nm wavelength Ar-Ion excitation source. The Ar-Ion source was preferred over 633nm wavelength He-Ne excitation source because the penetration depth of the 488nm source is lower compared to the 633nm source [38]. This was ideal for 300nm thick films, prepared in this experiment, since the perturbation of the spectroscopic data due to the backscattered Raman photons from the substrate can be significantly mitigated through this approach. During the measurements the laser intensity onto the substrate surface was reduced to 10% of the maximum intensity, to approximately 0.27 mW, in order to prevent crystallization of the thin film silicon.

The acquired Raman curves were then deconvoluted in order to calculate the volume fraction of the crystalline and amorphous phases inherent within the nc-Si:H thin film respectively. Based on how one deconvolutes the Raman curve there exist two different methods for calculating the volume fraction of the respective phases. For naming convention they will be called *two peak* and *three peak methods* respectively.

In the ***two peak method*** the Raman curves are deconvoluted at 480 cm^{-1} and 520 cm^{-1} TO respectively and the peak intensities, $\boldsymbol{I_{480}}$ and $\boldsymbol{I_{520}}$, are inserted into the following equation in order to calculate the crystallinity:

$$X_c = \frac{(I_{520})}{(I_{520} + \chi I_{480})} \qquad \textbf{(8)}$$

Where, the *correction factor* (χ) is multiplied with the amorphous Si TO peak in order to account for the larger scattering cross section in amorphous phase compared to crystalline phase [38 – 40]. For demonstration purposes the Raman spectra for nc-Si:H thin film deposited with 98.57% hydrogen dilution ratio is shown in **Figure 3.2** along with the deconvoluted Gaussian curves with peaks centered at 480 cm^{-1} and 520 cm^{-1} TO respectively. A crystallinity of 71.93 % was obtained by plugging in the acquired peak intensities, I_{480} and I_{520} respectively, from the curve in the aforementioned equation.

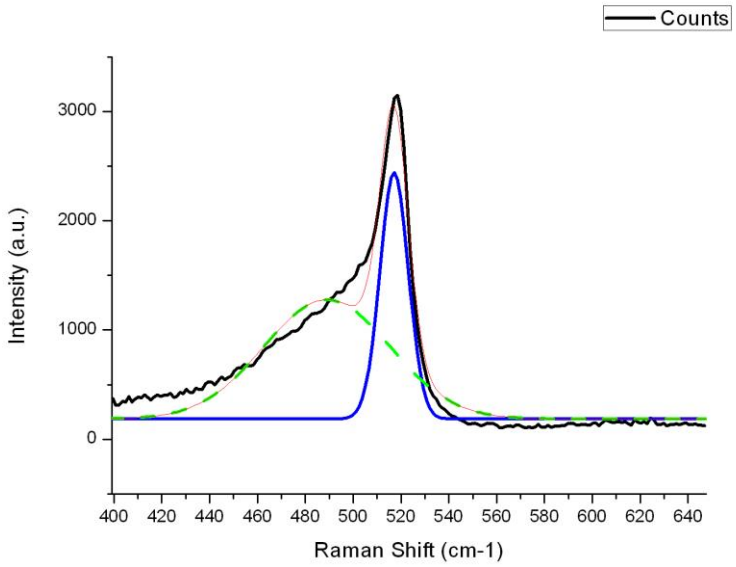

Figure 3.2: The Raman intensity graph of the nc-Si:H thin film deposited with 137.5 sccm (98.57%) hydrogen flow rate. The plot is deconvoluted at 480 cm^{-1} and 520 cm^{-1} transverse optical, which represents the amorphous and crystalline phases in nc-Si:H.

In the ***three peak method*** the Raman curves are deconvoluted at 480 cm^{-1}, 500 cm^{-1}, and 520 cm^{-1} TO respectively and the areas of the three Gaussian curves centered at the aforementioned TO values are inserted into the following equation in order to calculate the crystallinity:

$$X_c = \frac{(A_{520} + A_{500})}{(A_{520} + A_{500} + A_{480})} \quad \textbf{(9)}$$

Here, $\mathbf{A_{520}}$, $\mathbf{A_{500}}$, and $\mathbf{A_{480}}$ are the area under the deconvoluted Gaussian curves whose peak values are located at 480 cm^{-1}, 500 cm^{-1}, and 520 cm^{-1} TO respectively [13]. Although, both these methods are equally established, for this report the *two peak method* was used to calculate the crystalline volume fraction.

ii. Glancing angle X-Ray diffraction (XRD) spectroscopy:

Aside from the use of Raman Spectroscopy, which qualitatively provides information on the volume fraction of crystalline and amorphous phases in the thin film silicon, glancing angle XRD spectroscopy is most often used concurrently with Raman spectroscopy to determine the

predominant crystal orientation, grain size, stress etc. of the thin film. This is particularly important since the predominance of certain orientations have been shown to yield improved electronic conductivity in nc-Si:H and has been an object of interest by the research community [41].

The glancing angle XRD's of the deposited thin films in this research were performed using PANalytical X'Pert PRO Materials Research Diffractometer (MRD) with a Cu Kα emission source. In this section a theoretical outline of XRD and the glancing angle XRD setup will be briefly overviewed before explaining the improvements in conductivity for certain crystal orientations.

a. General theoretical overview of XRD:

X-Ray diffraction occurs due to the comparable dimensions of the X-ray wavelength and the lattice spacing. The incident beam interacts with the electronic cloud of the lattice atoms and is elastically reradiated (frequency remains the same) [42]. The reradiated waves from each lattice atom interfere constructively or destructively with other reradiated waves (**Figure 3.3**). This results in a diffraction pattern similar to the famous double slit experiment, except in this case the lattice behaves similar to a 3D diffraction grating instead of 1D.

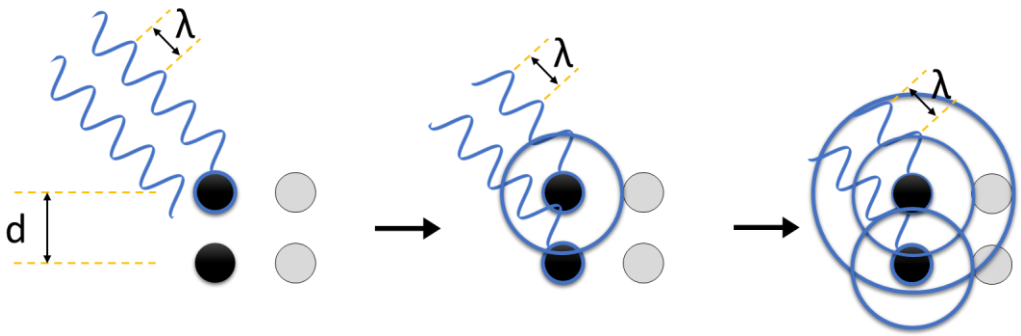

Figure 3.3: Visual depiction of the X-Ray interaction with the lattice atoms in the crystal [42]. Interplanar distance (d) is indicated.

Since the lattice behaves similar to a 3D diffraction grating, the peak intensity over an angular range of incident X-ray beams on a family of planes registers a maximum for a specific incident angle. This can be identified using Bragg's equation,

$$n\lambda = 2d\sin\theta \qquad \textbf{(10)}$$

Where, **n**, **d**, and **θ** are the *wavelength order*, *interplanar distance*, and *angle of incidence* respectively [43]. The formulation states that the constructive interference can only occur when the path length difference between two incident parallel beams, scattered from adjacent parallel planes separated by a distance d, are an integer number of the λ (**Figure 3.4**). Furthermore, for different interplanar distances, d, the condition is satisfied at specific 2Θ angles. Thus the specific plane that is contributing towards diffraction can be easily identified.

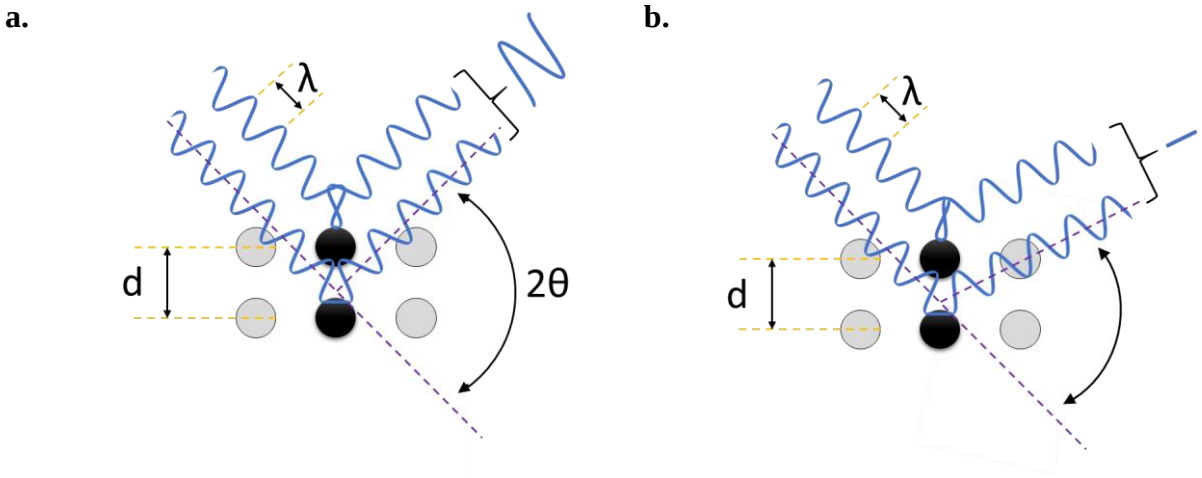

Figure 3.4: Schematic diagram of the **(a)** constructive and **(b)** destructive interference of the scattered X-Rays from two parallel lattice planes [42].

b. Glancing angle XRD setup:

As a result of the thickness range of thin films, maximum of 2 μm, a regular XRD setup is impractical, since the X-rays would penetrate through the film and be scattered by the substrate [44]. Thus the information about the crystal orientation and the texture of the material would be

overshadowed by the signal received from the substrate. This would make the data hard to configure and its practical value would become redundant.

Glancing angle geometry is used to avoid X-ray signals from the substrate [44]. In this technique the incident beam from the stationary X-ray source makes a very small angle with the substrate surface, typically 1^{o} to 3^{o} (**Figure 3.5**) [44]. As a result the path length of the X-Ray beam increases through the film. This automatically increases the thin film signal to background ratio of the scattered X-rays from the substrate [44]. Furthermore, the geometry is simplified by only allowing the detector to move over the angular range [44]. This implies that the incident angle, the beam path length, and the irradiated area remain constant as well [44].

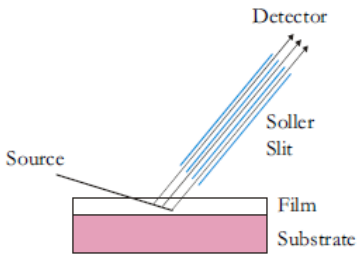

Figure 3.5: Simplified schematic of the glancing angle XRD analysis [43]. Image acquired from reference [43].

In addition to the glancing geometry, Soller slits, are used in front of the detector in order to only allow approximately parallel beams to pass through [44]. This reduces the sensitivity to sample displacement from the rotation axis [44]. The figure depicted here is an oversimplified diagram of the thin film Goniometer geometry. For a detailed overview of the thin film Glancing Angle XRD analysis one may look up the surveys on this technique by Sergey Stepanov [45], B. K. Tanner et al. [46], P. Dutta [47] etc.

c. Correlation between crystal orientation and improved nc-Si:H thin film solar cell parameters:

Three predominant crystal orientations, (111), (220), and (311), are commonly observed for the powder XRD of c-Si. The peak height intensity ratio of these crystalline planes is 1:0.55:0.3 respectively [48]. Similar, crystal orientations are observed for nc-Si:H thin films as well.

However, unlike powder XRD of silicon, the crystalline peak intensity ratios can be varied for nc-Si:H. This implies that the grain number densities or sizes, with specific orientations, can be increased or decreased in the resultant nc-Si:H film.

Under particular PECVD deposition conditions, near the a-Si:H to nc-Si:H transition region, a higher (220) peak intensity is observed compared to that for highly crystalline nc-Si:H [41, 49]. In some cases it has been observed that the I(220)/I(111) peak height ratio is greater than 1 [41, 49]. This stems from the larger volume fraction of (220) oriented grains compared to (111) oriented grains in the nc-Si:H thin film [41, 49, 50]. More specifically, it has been reported that under such conditions, (220) grain sizes are longitudinally larger compared to (111) [48].

The prevalence of the longitudinally large (columnar) grains near the transition region is desirable for solar cell applications. This, implies that the charge carriers, whose conduction path is perpendicular to the substrate in the nc-Si:H solar cells, will witness fewer grain boundaries under (220) oriented grains than it did for (111) oriented grains. Additionally, the predominance of the amorphous volume fraction serves to passivate the grain surface. The sum combination of these two phenomena serves to reduce bulk recombination and/or field losses in the thin film solar cell [41]. This increases the V_{oc} and FF of the nc-Si:H solar cells, respectively.

iii. Electronic properties:

The electronic properties of the nc-Si:H thin films were measured by characterizing the coplanar conductivities of the films. This was achieved by depositing seven Aluminum (Al) contact pads, 0.2 cm x 2 cm, with 0.1 cm spacing between them [31]. The pads were deposited by shadow masking the nc-Si:H film during Aluminum deposition in the WLOS MVSystems Cluster Sputtering machine. Thereafter the electrical measurements were performed on the SIGNATONE S-1060R probe station and the I-V characteristics were measured using AGILENT 4155C Semiconductor Parameter Analyzer.

During the Photo I-V measurements a Halogen lamp was used. The lamp was turned on for 15 – 20 minutes, prior to performing the measurements, in order for it to stabilize and warm up. The intensity of the light source was measured using SOLAR Light Co. PMA 2200

Photometer/Radiometer and was set around 105 $\pm$ 5 mW/cm^2 on the nc-Si:H substrate surface. In order to prevent the chuck of the probe station from warming up, ice bags were placed on the chuck beside the samples. The σ_{ph} and σ_D of the films were measured using the following equation:

$$\sigma_{ph} \quad or \quad \sigma_D = \frac{I}{V} \times \frac{D}{l \times t} \tag{11}$$

Where, ***D*** is the *distance* between individual electrodes (1 mm), ***t*** is the *thickness* of the nc-Si:H thin films (300 nm), ***l*** is the *length* of the individual electrodes (2 cm), ***V*** is the applied *voltage* and ***I*** is the measured *current* [31].

3.1.3 Phase 2: Depositing intrinsic nc-Si:H thin film via p-PECVD

Optimum crystallinity and electronic property was observed for nc-Si:H thin film deposited via cw-PECVD at 98.57% hydrogen dilution ratio. As a result, this recipe was further used for depositing thin films using p-PECVD. During the pulsing operation the duty cycles of the pulses were kept at 50% and the peak power was set to 10 W so that the average power of both processes, cw and p-PECVD, were equal at 5 W. Additionally, all the deposition parameters developed in cw-PECVD, *pressure*, *power*, *substrate temperature*, and *silane and hydrogen flow rate*, were kept constant. Six samples with the following pulsing frequencies of 0.2, 1, 5, 10, 25, and 50 kHz respectively were deposited for 1.5 hrs for deposition rate measurement. The deposition rate was calculated similar to that for nc-Si:H films fabricated using cw-PECVD and is summarized in **Table 3.2** (**Appendix: Phase 2**).

Table 3.2: Thin film silicon *phase*, *thickness* (Å), and *deposition rate* (Å/s) for different pulsing frequencies (0.2, 1, 5, 10, 25, and 50 kHz) at 50% duty cycle. The films were deposited for 1.5 hrs. The deposition rate of the nc-Si:H sample fabricated via cw-PECVD at 98.57% hydrogen dilution ratio is also listed for comparison purposes.

Sample	Pulse Frequency (kHz)	Pulse Period (µs)	Phase	Film Thickness (Å)	Deposition Rate (Å/s)
Sam013 (a & b)	-	-	**Crystalline**	-	**0.234 + 0.004**
Sam020 (a & b)	0.2 (200Hz)	5000 (5ms)	Crystalline	1068 + 37	0.198 + 0.007
Sam021 (a & b)	1	1000 (1ms)	Crystalline	1076 + 37	0.199 + 0.007
Sam022 (a & b)	5	200	Crystalline	1062 + 23	0.197 + 0.004
Sam023 (a & b)	10	100	Crystalline	1081 + 17	0.200 + 0.003
Sam024 (a & b)	25	40	Crystalline	1046 + 35	0.194 + 0.006
Sam025 (a & b)	50	20	Crystalline	1062 + 23	0.197 + 0.004
Avg. D.R./Time	-	-	-	-	0.198 + 0.005

The calculated deposition rates were then used to deposit 300nm thick films at the same pulsing frequencies. The upper and lower limits of the pulsing frequency, used in this report, were determined as follows:

1. The ***upper limit*** was set below the the *maximum pulsing frequency* beyond which the observed (displayed) peak power was higher than the input peak power. Although the maximum pulsing frequency of the power source was 100 kHz, at 10 W peak power the maximum achievable pulsing frequency was approximately 55 kHz. Thus 50 kHz was chosen as the upper limit of the pulsing frequency.
2. The ***lower limit*** was set above the *minimum pulsing frequency* below which the plasma is unsustainable between ON and OFF cycles. This is because the system does not have the critical amount of electrons to induce plasma ignition. The lowest pulsing frequency achieved, for the specific set of PECVD parameters used in this research, was approximately 0.1 kHz. As a result 0.2 kHz was chosen as the lower limit of the pulsing frequency.

3.1.4 Phase 2: Characterizing intrinsic nc-Si:H thin film deposited via p-PECVD

Similar characterization procedures to films deposited using cw-PECVD, namely Raman crystallinity, Surface Glancing XRD, and Conductivity Measurements, were carried out for the 300 nm thick nc-Si:H films deposited using p-PECVD.

i. Activation Energy (E_A) Measurement:

The E_A of the nc-Si:H thin films, deposited via p-PECVD, were calculated after measuring the dark I-V characteristics at 25°C, 50°C, and 75°C respectively. This was accomplished by using the CASCADE MICROTECH probe station with a TEMPTRONIC corporation T3000 temperature controller and AGILENT 4155C Semiconductor Parameter Analyzer. The observed σ_D at the aforementioned temperatures were plotted as a function of 1/T in the Sma4Win software. The plot was then exponentially fit and the E_A was measured using the *Arrhenius Equation*, which is expressed as follows:

$$\sigma_D = \sigma_o . e^{-\left(\frac{E_A}{K_B T}\right)} \quad \textbf{(12 a)}$$

$$\ln \sigma_D = \ln \sigma_o - \left(\frac{E_A}{K_B}\right)\left(\frac{1}{T}\right) \quad \textbf{(12 b)}$$

Where, $\boldsymbol{\sigma_o}$, $\mathbf{K_B}$, and **T** are *constant*, *Boltzmann constant*, and *temperature* respectively [31].

ii. Vacuum Annealing:

The nc-Si:H samples fabricated using p-PECVD were then vacuum annealed (approximately 26 in.Hg) at 150°C for six hours. Thereafter it was subsequently cooled in the same environment for approximately two and half hours by lowering the oven temperature to 25°C. The samples were then quickly taken out of the chamber and their dark and photo I-V characteristics were measured using AGILENT 4155C Semiconductor Parameter Analyzer on the SIGNATONE S-1060R probe station. Similar light source and intensity, as mentioned above for the samples deposited using cw-PECVD, was employed during photo I-V measurements. Two set of nc-Si:H samples were annealed in the same oven in order to finish the annealing

process fairly quickly. Additionally, two different annealing ovens, BCB curing Oven and Hotpack Vacuum Oven, were utilized, with four of the samples annealed in the former and two in the later respectively.

3.2 Thin Film nc-Si:H solar cell

3.2.1 Thin Film nc-Si:H Solar Cell Design

The thin film solar cells were fabricated in superstrate configuration so as to avoid the complication of fabricating and optimizing thick high quality Transparent Conductive Oxide (TCO) and making external contacts. In superstrate configuration, Asahi tin oxide (SnO_2) TCO coated square glass wafers, 10cm x 10cm, were used as the transparent substrate. A 10nm ZnO-TCO was deposited as a transparent passivating layer so that the SnO_2-TCO, which is reactive to hydrogen plasma, was protected. Thereafter, a 20 nm of p^+-nc-Si:H p – layer, 600nm i – layer , 30 nm n^+-a-Si:H n – layer and Al contact pads were deposited in sequence in order to fabricate the p-i-n solar cells.

Three thin film solar cells were fabricated in total for this research. These were namely a-Si:H test cell and the two nc-Si:H cells with absorber layers deposited either via cw or p-PECVD. The a-Si:H test cell with 400 nm a-Si:H i – layer was fabricated in cw-PECVD so as to investigate if it demonstrated the characteristic J-V curve of a solar cell under photo illumination. This was because the other components of the p-i-n cells, i.e. TCO, p – layer, n – layer, Al contacts, light management mechanisms, etc., were not optimized.

Following the successful observation of the characteristic J-V curve from the a-Si:H test cell, 600nm thick i – layer nc-Si:H cells were fabricated using the optimized thin film recipes from the cw and p-PECVD processes respectively. As the aim of the research was to compare the quality of nc-Si:H fabricated from both cw and p-PECVD processes, the usual thickness range of 1-2 μm for nc-Si:H i – layers were not used.

3.2.2 Thin Film nc-Si:H Solar Cell Fabrication

Prior to the fabrication of the thin film solar cells, the individual components of the solar cell, ZnO-TCO passivating layer, p^+ nc-Si:H, and n^+ a-Si:H, were individually deposited on 3 inch diameter Eagle 2000 glass wafers for deposition rate characterization. The recipes for the deposited films are outlined in **Table 3.3**.

Table 3.3: Thin film recipes for the individual components of the solar cell in the R-to-R system.

Film	Flow Rate (sccm)					Temp. (ºC)		Pressure (mTorr)	Power (W)	Deposition Time (sec)
	Ar	SiH_4	H_2	B_2H_6	PH_3	G	HW			
ZnO	30	–	–	–	–	–	250	5	300	1200
p^+ nc-Si:H	–	1	200	1.5	–	250	250	900	6	3600
n^+ a-Si:H	–	20	–	–	3	250	250	400	2	600

The deposition rates were measured similar to the method outlined previously for the intrinsic nc-Si:H thin film. Except during the etching step of ZnO-TCO, instead of RIE, the films were dipped in 0.5% HCl to H_2O solution.

Thereafter the thin film solar cells were fabricated sequentially as mentioned above. Apart from the sequential deposition of the films, 20 mins of a-Si:H dummy run was performed between P^+ nc-Si:H and i – layer fabrication process in order to prevent the device from being contaminated by p-type dopants from the wall. This step was carried out after transferring the substrate to the LL from the PECVD chamber.

Finally, after fabricating the n^+ a-Si:H layer, shadow masks with approximately 5.6 mm diameter openings were used to deposit Al in the WLOS sputtering chamber. This led to the production of cells with an effective area of approximately 0.25 cm^2. In total 33 individual cells were fabricated per device. The solar cell devices were then annealed in vacuum for six hours at 150ºC so that the Al contact pads made proper contact with the n – layer.

3.2.3 Thin Film nc-Si:H Solar Cell Characterization

Thin wires were glued on to the Al back contact of 5 of the cells and the exposed SnO_2 TCO (top contact) near the substrate edge using H20E EPO-TEK silver conductive epoxy. This was

done in order to make the anode (positive) and the cathode (negative) contacts of the cells, respectively. Thereafter, the epoxy was cured by annealing the sample at 90^{o}C and the J-V characteristics of the thin film solar cells, a-Si:H test cell and both the nc-Si:H cells (cw and p-PECVD), were measured under AM1.5 100 mW/cm^{2} solar irradiation. Subsequently, the EQE of the devices was measured for the spectral range of 300nm to 800nm.

After discussing the experimental procedures, the observed experimental results will now be discussed.

Chapter 4: Results and Discussion

In this section, the characterization results of nc-Si:H films fabricated from cw and p-PECVD will be outlined and compared. These include deposition rate, crystallinity, I(220)/I(111) XRD peak ratio, and σ_{ph} and σ_D conductivity of the nc-Si:H films respectively. Thereafter, the J-V and EQE measurements for the nc-Si:H solar cells with absorber layers fabricated from the cw and p-PECVD processes will be discussed.

4.1 nc-Si:H Deposition Rate

In the initial stages of nc-Si:H thin film characterization, the deposition rates of the thin films deposited via cw and p-PECVD were characterized in order to obtain uniform thick films for Raman, XRD, and Conductivity measurements. During thin film silicon deposition via cw-PECVD, it was observed that the deposition rate decreased from 0.303 $\pm$ 0.004 Å/s to 0.16 $\pm$ 0.003 Å/s with increasing hydrogen dilution ratio from 98% to 99.01% (**Figure 4.1 a**).

This reduction in the deposition rate with increasing hydrogen dilution ratio was attributed to the increase in hydrogen etching during film growth. The flux of atomic hydrogen onto the growing thin film surface cleaved strained Si-Si bonds and produces silane (*Etching Model, pg. 24*) [13, 14]. The product silane molecules then returned back to the plasma [13, 14].

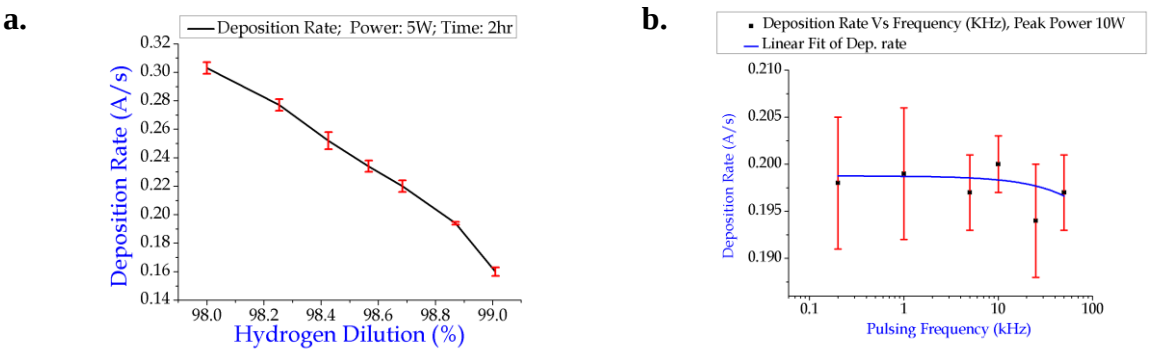

cw-PECVD **p-PECVD**

Figure 4.1: Thin film silicon deposition rate (Å/s) as a function of **(a)** hydrogen dilution ratio from 98.0% to 99.01% in cw-PECVD and **(b)** pulsing frequency between 0.2 to 50 kHz at 50% duty cycle for 98.57% hydrogen dilution ratio.

Following the characterization of the films in cw-PECVD, the thin film recipe with hydrogen dilution ratio of 98.57% was qualitatively chosen based on high crystallinity, XRD I(220)/I(111) peak ratio, and photoresponsivity (σ_{ph} / σ_D). The deposition rate observed at 98.57% hydrogen dilution ratio was 0.234 $\pm$ 0.004 Å/s. This recipe was then further subjected to p-PECVD at 0.2, 1, 5, 10, 25, 50 kHz pulsing frequency and 50% duty cycle respectively. The average power of both the processes was kept the same at 5W. It was observed that the deposition rate of the nc-Si:H thin films were independent of the specified pulsing frequency, with an average deposition rate of 0.198+0.005 Å/s (**Figure 4.1 b**). Hence the deposition rate achieved using p-PECVD was lower than that achieved in cw-PECVD.

To investigate the cause behind the decrease in the deposition rate during pulsing operation, the 98.57% hydrogen dilution ratio recipe was used to deposit thin film in cw-PECVD at 10 W average power (this was the *peak pulse power* during pulsing operation, *Section 3.1.3*). A deposition rate of 0.37 $\pm$ 0.01 Å/s was observed. This was roughly twice as that obtained from p-PECVD with 10 W peak power. From this it was deduced that the decrease in the deposition rate in p-PECVD was related to the 50% duty cycle.

It is worth noting that the observed deposition rate was not exactly half, but a little bit larger. This was related to the higher dissociation rate of silane at the onset of plasma Ignition from OFF

to ON. This occurred due to the high electron temperature at the moment of plasma ignition, which subsequently decreased with increasing electron density [51].

4.2 Raman Spectroscopy

The Raman crystallinity of the 300nm thick nc-Si:H films deposited using cw-PECVD and p-PECVD are shown in **Figure 4.2 (a)** and **(b)**.

a.

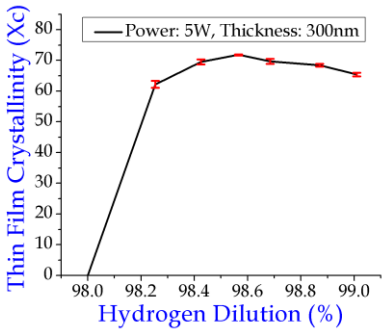

cw-PECVD

b.

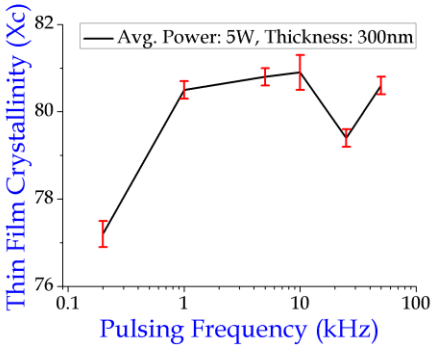

p-PECVD

Figure 4.2: Thin film silicon crystallinity as a function of **(a)** hydrogen dilution ratio from 98% to 99.01% and **(b)** pulsing frequency from 0.2 to 50 kHz at 50% duty cycle for 98.57% hydrogen dilution ratio. *Two peak method* was used to calculate the crystallinity of the films.

It was observed that the crystallinity of the cw-PECVD samples rose to 71.8% at 98.57% hydrogen dilution ratio and then slightly dropped to 65.4 $\pm$ 0.6 % at 99.01% (**Table 4.1**). This increase in the crystallinity with increasing hydrogen dilution ratio resulted from *two concurrent processes*:

1. ***High hydrogen flux density*** onto the growing thin film surface selectively etched strained (weak) Si-Si bonds. This increased the number density of energetically favorable vacant sites, on the film surface, to which other SiH_3 adatoms could attach and form strong Si-Si bonds (*The Etching Model, pg. 24*) [14].
2. ***Uniform surface coverage via hydrogen atoms*** on the film surface increased the frequency of hydrogen exchange reactions. This raised the localized heat on the surface,

which further increased the diffusion length of the SiH_3 adatoms. As a result the probability of these adatoms locating energetically favorable sites, to form strong Si-Si bonds, were greatly enhanced. Continuous repetition of this process led to the formation of a rigid crystalline structure (*The Surface Diffusion Model, pg. 23-24*) [14].

Table 4.1: The nc-Si:H crystallinity (*Two peak method*) for hydrogen dilution ratio from 98% to 99.01% (cw-PECVD) and pulsing frequency from 0.2 to 50 kHz at 50% duty cycle (p-PECVD).

cw-PECVD			**p-PECVD**		
Sample	**Hydrogen Dilution Ratio**	**Sample Crystallinity (Two Peak Method)**	**Sample**	**Pulsing Frequency (kHz)**	**Sample Crystallinity (Two Peak Method)**
Sam014 (a & b)	98.25%	62.2 ± 1.1 %	**Sam020 (c & d)**	0.2	77.2 ± 0.3 %
Sam015 (a & b)	98.43%	69.5 ± 0.8 %	**Sam021 (c & d)**	1	80.5 ± 0.2 %
Sam016 (a & b)	**98.57%**	**71.8 ± 0.2 %**	**Sam022 (c & d)**	5	80.8 ± 0.2 %
Sam017 (a & b)	98.68%	69.7 ± 0.8 %	**Sam023 (c & d)**	10	80.9 ± 0.4 %
Sam018 (a & b)	98.87%	68.4 ± 0.5 %	**Sam024 (c & d)**	25	79.4 ± 0.2 %
Sam019 (a & b)	99.01%	65.4 ± 0.6 %	**Sam025 (c & d)**	50	80.6 ± 0.2 %

It was considered that the slight drop in the crystallinity, for hydrogen dilution ratios exceeding 98.57%, resulted from the depletion of SiH_4 molecules in the plasma. This occurred due to the low silane flow rate (2sccm). Thus the reactive species formed within the plasma could not react with other SiH_4 molecules or radicals [14]. As a result, during the deposition process, these reactive species were automatically incorporated in the film [14].

Additionally, the higher atomic hydrogen flux density on the film surface not only etched the film but also reacted with the surface adatoms. This increased the number density of vacant sites that were included in the resultant film due to the lack of SiH_3 precursors available take up these sites. The aforementioned phenomena led to a decline in the crystallinity of the film [14].

The recipe transfer from cw to p-PECVD at 98.57% hydrogen dilution ratio led to a rise in the crystallinity up to a maximum of 80.9 $\pm$ 0.4% at 10 kHz pulsing frequency (**Figure 4.2 b**). This observed rise in crystallinity was related to *two simultaneous processes*:

1. ***Higher peak power*** during plasma ON time. This resulted in the generation of larger densities of SiH_3 film precursors and atomic hydrogen.
2. ***Removal of negative ions*** and ***low life time species*** during plasma OFF time [23, 52]

The sum combination of the aforementioned processes increased the crystallinity of the nc-Si:H film under p-PECVD operations [14, 23, 52].

4.3 I(220)/I(111) XRD peak ratio

One of the key ways of reducing photocarrier losses, in the nc-Si:H solar cell bulk, is to reduce the density of grain boundaries perpendicular to the current conduction path [41]. This is achieved by manipulating the deposition conditions in order to obtain elongated grains oriented parallel to the direction of current conduction [49].

To elucidate briefly, the microstructure of nc-Si:H is composed of silicon nanocrystals, closely packed together to form micron sized conglomerates, surrounded by an amorphous matrix [48]. The volume fraction of these crystalline conglomerates and amorphous tissue vary based on the deposition conditions, e.g. hydrogen flow rate, power etc. It has been observed that for highly crystalline deposition conditions, not only do the conglomerate volume fraction in the bulk increases steeply, but it also raises the density of grain boundaries, voids, and cracks in the resultant thin film as well. This leads to carrier losses and leaves the resultant material prone to post fabrication impurity contamination from the ambient [36].

Conversely, near the transition from a-Si:H to nc-Si:H growth, it has been reported that the nanocrystals, instead of being closely packed into conglomerates, are dispersed in the amorphous matrix. This specific microstructural configuration is of device research interest, since the

prevalence of the amorphous tissue serves to passivate the dangling bonds on the nanocrystal surface. Furthermore, under certain conditions, high density of elongated nanocrystals can be observed near the transition region, as well [49]. The sum combination of these effects, yield larger V_{oc} and FF in the finished solar cell device [36].

These elongated grains, near the transition region, are (220) oriented [49, 53]. Consequently, significant research has been undertaken in order to produce (220) textured films [24, 41, 55]. Toyoshima et al., experimenting on the nature of grain orientation in nc-Si:H, concluded *two primary factors* that control the predominance of (220) oriented crystals [55]. They are:

1. ***Substrate surface temperature*:** A rise in the substrate surface temperature favors (220) orientation. This is because, at higher substrate temperatures, the growth rate of (220) grains are far larger than (111) grains [39, 55]. This leads to the growth of larger (220) crystals and hence the (220) XRD peak intensity increases compared to (111) [55].
2. ***Hydrogen dilution ratio:*** An increase in the hydrogen dilution ratio in the plasma increases the volume fraction of (111) grains [55]. During the nc-Si:H growth, a substantial preference of (111) nucleate density over (220) is observed regardless of the substrate temperature (<300ºC) [49]. The specific reason behind this preference is not yet understood [55]. Additionally, increasing the hydrogen dilution ratio further decreases the (111) and (220) nucleation density [55]. This results from the hydrogen induced rise in the SiH_3 adatom mobility, which has an inverse relationship with the nucleation density [55]. The overall effect leads to a reduction in the volume fraction of (220) grains due to their already low nucleate density compared to (111) [55].

Hence, during thin film characterization, the film recipe that demonstrated higher XRD I(220)/I(111) peak ratio was sought.

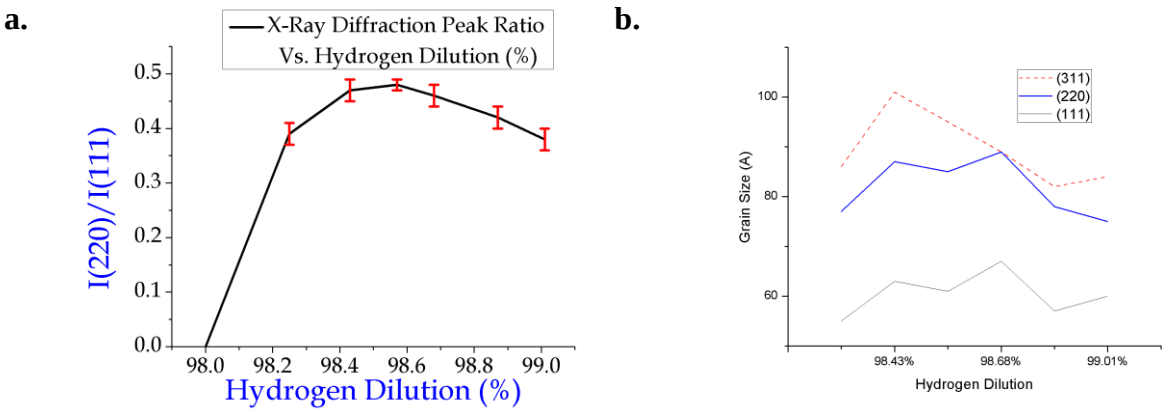

Figure 4.3: The variation of nc-Si:H **(a)** XRD I(220)/I(111) peak ratio and **(b)** grain size (Å) with increasing hydrogen dilution from 98% to 99.01%. The films were deposited in cw-PECVD.

The I(220)/I(111) for the nc-Si:H thin films, with varying hydrogen dilution ratios, are plotted in **Figure 4.3 (a)**. It was observed that the I(220)/I(111) was less than unity for all the samples. This implied that the volume fraction of (111) grains in the thin film bulk was larger than (220) grains, even though, from the Full Width Half Maximum (FWHM) measurements, it was observed that the grain sizes of (220) grains (~7-9nm) were larger than (111) grains (~5-6nm) (**Figure 4.3 b**).

The below unity of the I(220)/I(111) resulted from the low substrate temperature (150^{o}C for this report) during the film deposition process [55]. It was considered, based on Toyoshima et al. [55], that (111) nucleation density at this temperature was far larger than (220). This led to the observation of larger (111) crystalline volume fraction, and hence a higher peak height, compared to (220). Moreover, the growth rate of the (220) crystals were greater than (111) crystals. As a result the (220) grains were larger than (111).

Additionally, It was observed that the I(220)/I(111) increased to 0.48 at 98.57% hydrogen dilution ratio, from the onset nc-Si:H phase, and then subsequently decreased to 0.39 at 99.01%. Hence, there was an increase in the volume fraction of (220) grains near the a-Si:H to nc-Si:H transition region, which subsequently decreased with increasing hydrogen dilution ratio beyond 98.57%.

The rise in the (220) volume fraction, from the transition region until 98.57% hydrogen dilution ratio, resulted from the concurrent increase in the (111) and (220) nucleation density. Further increasing the hydrogen dilution ratio beyond this value sharply decreased the nucleation density of both (111) and (220) crystals [55]. However, since the (111) nucleation density were far larger than (220) at 150^{o}C, the drop in the (111) and (220) nucleation density further reduced the (220) volume fraction [55].

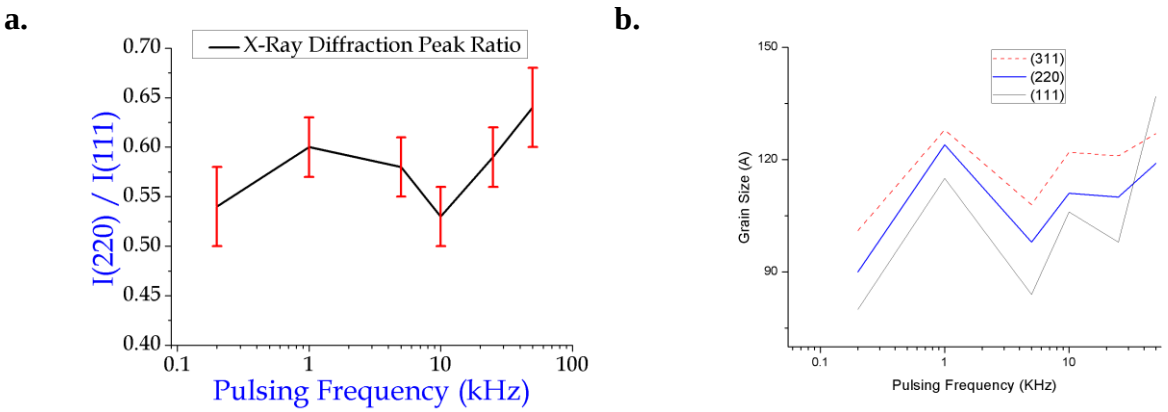

Figure 4.4: The nc-Si:H **(a)** XRD I(220)/I(111) peak ratio, and **(b)** grain size (Å) as a function of the pulsing frequency from 0.2 to 50 kHz at 50% duty cycle for 98.57% hydrogen dilution ratio.

The I(220)/I(111) and grains sizes for the p-PECVD samples were 0.54-0.64 and ~ 8-13 nm respectively (**Figure 4.4 a** and **b**). This was higher than the I(220)/I(111) and the grain sizes of 0.48 and ~ 6-9 nm respectively achieved from the cw-PECVD sample fabricated at 98.57% hydrogen dilution ratio. However, the I(220)/I(111) for p-PECVD is still less than unity. This resulted from the low substrate temperature (~150ºC) during the fabrication process [55]. Furthermore, no trend in the I(220)/I(111) were observed within the specified pulsing frequency range (0.2 – 50 kHz). Rather the mean values of the peak ratios at each pulsing frequency were observed to lie within the respective error limits of each other.

Having said that, the rise in the values of the I(220)/I(111) and grain sizes for the p-PECVD samples, over what was observed using cw-PECVD, was related to the higher flux density of the SiH_3 film precursors and the atomic hydrogen flux onto the substrate surface. It was considered

that the larger density of SiH_3 precursors increased the growth rate of all nucleates, (111), (220), and (311), respectively. This led to the observation of a stronger (220) XRD peak intensity and larger grain sizes for all three set of grains.

Additionally, excess atomic hydrogen flux onto the film surface increased the mobility of the precursors, which reduced the nucleate density. However, the reduction of the (220) nucleate density was offset by the high density of SiH_3 precursors produced during the Plasma ON time. This implied that the (220) volume fraction would be higher for p-PECVD, hence larger I(220)/I(111), compared to that observed for cw-PECVD nc-Si:H sample, for the same recipe.

4.4 Conductivity Measurements

As mentioned previously, the nc-Si:H microstructure is composed of nanocrystalline grains closely packed into conglomerates surrounded by an amorphous matrix [48]. This microstructural organization leads to an anisotropic behavior of the electronic transport properties in nc-Si:H [48]. Hence the carrier transport properties parallel to the substrate differ with the properties perpendicular to the substrate [48]. This is problematic, since in a p-i-n solar cell device structure the direction of carrier transport, in the absorber layer, is perpendicular to the substrate.

However, no proficient method exists, thus far, that can allow for the adequate measurement of the electronic transport properties in this direction. Hence any result obtained from the coplanar electronic measurements (parallel to the substrate) can only provide an estimate magnitude of the vertical carrier transport properties. Nevertheless, this anisotropy in electronic transport can be assumed negligible near the nc-Si:H and a-Si:H transition region [48]. This more or less stems from the uniform dispersion of nanocrystalline grains in the amorphous matrix within nc-Si:H. As a result, the coplanar conductivity measurement technique was used to determine the σ_{ph} and σ_D and photoresponsivity of the nc-Si:H thin films.

4.4.1 Coplanar Conductivity Measurement

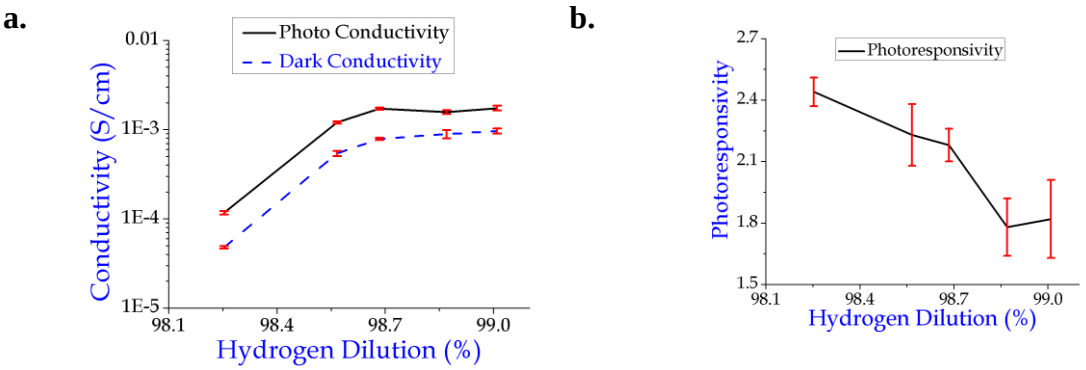

Figure 4.5: The nc-Si:H **(a)** σ_{ph} and σ_D and **(b)** the photoresponsivity as a function of hydrogen dilution ratio from 98% to 99%. The films were fabricated using cw-PECVD.

From the coplanar conductivity measurements, it was observed that the σ_{ph} and σ_D of the nc-Si:H thin films, fabricated using cw-PECVD, increased from 1.17E-04 $\pm$ 5E-06 S/cm and 4.8E-05 $\pm$ 2E-06 S/cm at 98.25% hydrogen dilution ratio to 1.74E-03 $\pm$ 1E-05 S/cm and 9.6E-04 $\pm$ 6E-05 S/cm at 99.01% hydrogen dilution ratio respectively, (**Figure 4.5 a** and **Table 4.2**). This observed rise in σ_{ph} and σ_D with increasing hydrogen dilution ratio resulted from the rise in crystallinity of the nc-Si:H thin films (**Figure 4.2 a**). This was because the σ_{ph} and σ_D were directly related to the electron (μ_n) and hole carrier mobilites (μ_p), which rose with increasing crystalline volume fraction [8].

Table 4.2: The nc-Si:H σ_D, σ_{ph}, and photoresponsivity for hydrogen dilution ratios from 98% to 99%.

Sample	Hydrogen Dilution ratio	σ_D (Ω^{-1} cm^{-1})	σ_{ph} (Ω^{-1} cm^{-1})	photoresponsivity (σ_{ph} / σ_D)
Sam014 (a & b)	98.25%	4.8E-05 $\pm$ 2-06	1.17E-04 $\pm$ 5E-06	2.44 $\pm$ 0.07
Sam015 (a & b)	98.43%	N/A	N/A	N/A
Sam016 (a & b)	**98.57%**	**5.4E-04 $\pm$ 4E-05**	**1.20E-03 $\pm$ 3E-05**	**2.23 $\pm$ 0.15**
Sam017 (a & b)	98.68%	7.9E-04 $\pm$ 2E-05	1.71E-03 $\pm$ 5E-05	2.18 $\pm$ 0.08
Sam018 (a & b)	98.87%	8.9E-04 $\pm$ 9E-05	1.57E-03 $\pm$ 7E-05	1.78 $\pm$ 0.14
Sam019 (a & b)	99.01%	9.6E-04 $\pm$ 6E-05	1.74E-03 $\pm$ 1E-05	1.82 $\pm$ 0.19

Similarly, the photoresponsivity of the nc-Si:H thin films demonstrated a maximum of 2.44 $\pm$ 0.07 at 98.25% hydrogen dilution ratio and then continually decreased to a value of 1.82 $\pm$ 0.19 at 99.01% (**Figure 4.5 b** and **Table 4.2**). The observed decrease in the photoresponsivity with increasing hydrogen dilution ratio was related to the shallower rise in σ_{ph} compared to σ_D. This

resulted from the relationship that σ_{ph} has with the τ and G [8]. Both of these quantities steadily decrease with the increasing crystallinity of the nc-Si:H thin film, offsetting the rise in the carrier mobilities (*Equations 2 & 3* and the related discussion on *pg.26-27*) [8]. The drop in photoresponsivity with increasing hydrogen dilution ratio was also observed by O. Vetterl et al. [12].

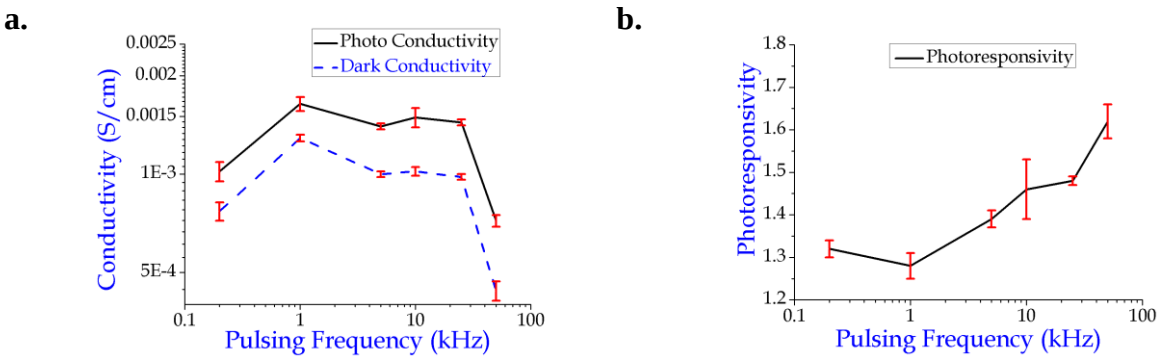

Figure 4.6: The nc-Si:H **(a)** σ_{ph} and σ_D conductivity and **(b)** the photoresponsivity with increasing pulsing frequency from 0.2 to 50 kHz at 50% duty cycle for 98.57% hydrogen dilution ratio.

The coplanar conductivity measurements of the nc-Si:H thin films, fabricated using p-PECVD, exhibited a twofold increase in the σ_D compared to the films fabricated using cw-PECVD. However, the σ_{ph} values remained approximately the same. A maximum σ_D and σ_{ph} value of 12.9E-04 $\pm$ 3E-05 S/cm and 1.64E-03 $\pm$ 8E-05 S/cm was observed at 1 kHz pulsing frequency respectively (**Figure 4.6 a** and **Table 4.3**).

Table 4.3: The nc-Si:H σ_D, σ_{ph}, and photoresponsivity for pulsing frequency from 0.2 to 50 kHz (p-PECVD). The same quantities for cw-PECVD at 98.57% hydrogen dilution ratio are shown for comparison purposes.

Pulsing Frequency (kHz)	σ_D (Ω^{-1} cm^{-1})	σ_{ph} (Ω^{-1} cm^{-1})	photoresponsivity (σ_{ph} / σ_D)
cw (98.57% H dilution)	**5.4E-04 $\pm$ 4E-05**	**1.20E-03 $\pm$ 3E-05**	**2.23 $\pm$ 0.15**
0.2	7.7E-04 $\pm$ 5E-05	1.02E-03 $\pm$ 7E-05	1.32 $\pm$ 0.02
1	12.9E-04 $\pm$ 3E-05	1.64E-03 $\pm$ 8E-05	1.28 $\pm$ 0.03
5	**10.0E-04 $\pm$ 2E-05**	**1.40E-03 $\pm$ 3E-05**	**1.39 $\pm$ 0.02**
10	10.2E-04 $\pm$ 3E-05	1.49E-03 $\pm$ 1E-04	1.46 $\pm$ 0.07
25	9.8E-04 $\pm$ 2E-05	1.44E-03 $\pm$ 3E-05	1.48 $\pm$ 0.01
50	9.9E-04 $\pm$ 2E-05	0.72E-03 $\pm$ 3E-05	1.62 $\pm$ 0.04

Although, the σ_D increased with the crystallinity of the nc-Si:H films fabricated using p-PECVD (**Figure 4.2 b**), the same association was not observed for σ_{ph}. It was speculated that for highly crystalline films, the high density of voids and cracks lead to a decrease in the τ and G. The sum combination of these two parameters offset the increase in the σ_{ph} that would have resulted from the rise in the carrier mobilities. Consequently, the observed photoresponsivity values were less than the values obtained for nc-Si:H film fabricated using cw-PECVD. A photoresponsivity high of 1.62 $\pm$ 0.04 at 50 kHz and a low of 1.32 $\pm$ 0.02 at 0.2 kHz was observed (**Figure 4.6 b**).

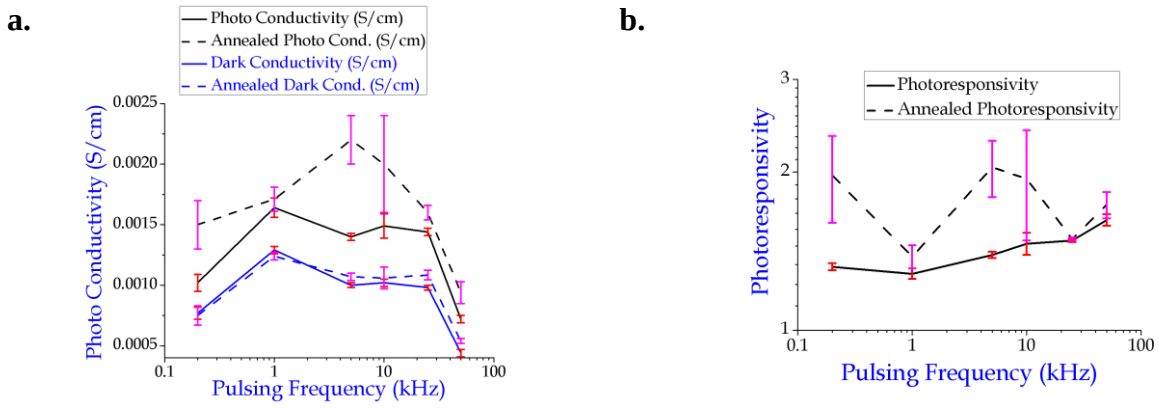

Figure 4.7: Comparison between the **(a)** σ_{ph} and σ_D and **(b)** the photoresponsivity of the nc-Si:H films as function of pulsing frequency before and after annealing. The nc-Si:H films were thermal annealed in vacuum (approximately 26 in.Hg) at 150°C for 6hrs. There after it was vacuum quenched for 2.5hrs.

In an attempt to reduce the σ_D and increase the σ_{ph}, the samples were thermal annealed in vacuum (approximately 26 in.Hg) for 6hrs and then vacuum quenched for 2.5 hrs. It was observed that σ_D approximately remained same, reaching a maximum of 12.4E-04 $\pm$ 3E-05 S/cm at 1 kHz pulsing frequency (**Figure 4.7 a** and **Table 4.4**). Conversely, the σ_{ph} of the nc-Si:H films improved and a maximum of 2.2E-03 $\pm$ 2E-05 S/cm was observed at 5 kHz pulsing frequency. This rise in σ_{ph} was not associated with the out gassing of the impurities, since the σ_D

would have decreased. Rather it was related to the improved contact between the Al pad and underlying nc-Si:H thin film.

Table 4.4: The nc-Si:H pre and post annealed σ_{ph}, σ_D, and photoresponsivity for pulsing frequency from 0.2 to 50 kHz at 50% duty cycle. The non-annealed σ_{ph}, σ_D, and photoresponsivity for cw-PECVD at 98.57% hydrogen dilution ratio are shown for comparison purposes.

Pulsing Frequency (kHz)	Dark Conductivity (Ω^{-1} cm^{-1})	Annealed Dark Conductivity (Ω^{-1} cm^{-1})	Photo Conductivity (Ω^{-1} cm^{-1})	Annealed Photo Conductivity (Ω^{-1} cm^{-1})	Photo responsivity	Annealed Photo sensitivity
CW	**5.4E-04 ± 4E-05**	**-**	**1.20E-03 ± 3E-05**	**-**	**-**	**2.23 ± 0.15**
0.2	7.7E-04 ± 5E-05	7.5E-04 ± 8E-05	1.02E-03 ± 7E-05	1.5E-03 ± 2E-05	1.32 ± 0.02	1.97 ± 0.37
1	12.9E-04 ± 3E-05	12.4E-04 ± 3E-05	1.64E-03 ± 8E-05	1.71E-03 ± 1E-05	1.28 ± 0.03	1.38 ± 0.07
5	**10.0E-04 ± 2E-05**	**10.7E-04 ± 3E-05**	**1.40E-03 ± 3E-05**	**2.2E-03 ± 2E-05**	**1.39 ± 0.02**	**2.04 ± 0.25**
10	10.2E-04 ± 3E-05	10.6E-04 ± 9E-05	1.49E-03 ± 1E-04	2.0E-03 ± 4E-05	1.46 ± 0.07	1.94 ± 0.46
25	9.8E-04 ± 2E-05	10.8E-04 ± 4E-05	1.44E-03 ± 3E-05	1.6E-03 ± 6E-05	1.48 ± 0.01	1.49 ± 0.01
50	9.9E-04 ± 2E-05	5.4E-04 ± 2E-05	0.72E-03 ± 3E-05	0.94E-03 ± 9E-05	1.62 ± 0.04	1.73 ± 0.10

As a result of the rise in σ_{ph}, after annealing, the photoresponsivity rose as well. A photoresponsivity high of 2.04 ± 0.25 at 5 kHz and a low of 1.38 ± 0.07 at 1 kHz was observed (**Figure 4.7 b** and **Table 4.4**). The photoresponsivity of the nc-Si:H samples were more or less constant for different pulsing frequencies, but they were still less than the non-annealed photoresponsivity of the nc-Si:H films fabricated using cw-PECVD. This resulted from the higher crystallinity of the nc-Si:H films fabricated using p-PECVD compared that of cw-PECVD.

In summary, the observed σ_D of the nc-Si:H films fabricated from both the cw and p-PECVD were on the order of 1E-04 – 1E-03 S/cm. This was three orders of magnitude higher than that reported by O. Vetterl et al. (1E-07 – 1E-06 S/cm) [12]. Similarly the measured σ_{ph} of the observed films were on the order of 1E-04 – 1E-03 S/cm compared to 1E-05 S/cm reported by the same author [12]. The resultant affect was that the photoresponsivities of the nc-Si:H films fabricated from both cw and p-PECVD were one to two orders of magnitude lower than the reported nc-Si:H films [12].

4.4.2 Activation Energy (E_A) Measurement

It was suspected that the high σ_D of the nc-Si:H thin films fabricated from cw and p-PECVD were related to the atmospheric indiffusion of H_2O, O_2, or N_2 into the films [36, 53]. Impurity indiffusion can perturb the measured data significantly if the films were not characterized instantaneously, at maximum within a day [36, 53]. E_A measurement is often carried out to verify the intrinsic nature of the nc-Si:H thin film. In this technique the E_A of the nc-Si:H film was determined by measuring the σ_D at different temperatures. Experimental studies on high quality intrinsic nc-Si:H thin films have revealed that films grown near the a-Si:H to nc-Si:H transition region have an E_A greater than 0.5 eV [48, 54].

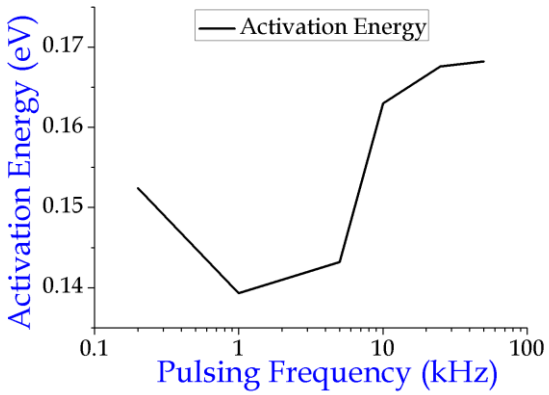

Figure 4.8: The activation energies (eV) of the nc-Si:H as a function of pulsing frequency from 0.2 to 50 kHz at 50% duty cycle for 98.57% hydrogen dilution ratio.

In order investigate the cause of high σ_D, the E_A measurements were performed on nc-Si:H films deposited using p-PECVD. An average E_A of 0.16 $\pm$ 0.01 eV for the nc-Si:H films was observed (**Figure 4.8**). This implied that the fabricated nc-Si:H films deposited using p-PECVD were not intrinsic. Rather they were mildly extrinsic. This confirmed the presence of impurities.

It was inferred that the nc-Si:H films were mildly n-type, since the common impurity atoms, such as O, N, C etc., in Silicon donate electrons to the CB [34]. High concentration of electrons in the CB converts the intrinsic nc-Si:H to n-type by moving the E_F closer to the E_C. This leads to a decrease in the E_A. Conversely, the σ_D of the nc-Si:H film increases, since it is directly

proportional to the mobility and concentration of the majority carriers [8]. This explained the unusually high σ_D on the order of 1E-04 – 1E-03 S/cm observed for the nc-Si:H films deposited using cw and p-PECVD. Meanwhile, the σ_{ph} of the contaminated films were affected by the decrease in the $\tau_{minority}$ of the films [8].

It was considered that the time delay in the characterization of the nc-Si:H thin film, which spanned between couple days to a week or so, due to the characterization system booking and setup, led to the indiffusion of impurities from the ambient [36]. Additionally, coplanar conductivity measurement was performed on the surface of the nc-Si:H film. However, this region would have had the highest concentration of impurities since it was directly exposed to air. Thus the measured σ_D was biased by the high concentration of impurities on the top surface [53].

4.5 J-V and EQE Measurements of the nc-Si:H cell with absorber layer prepared via cw and p-PECVD

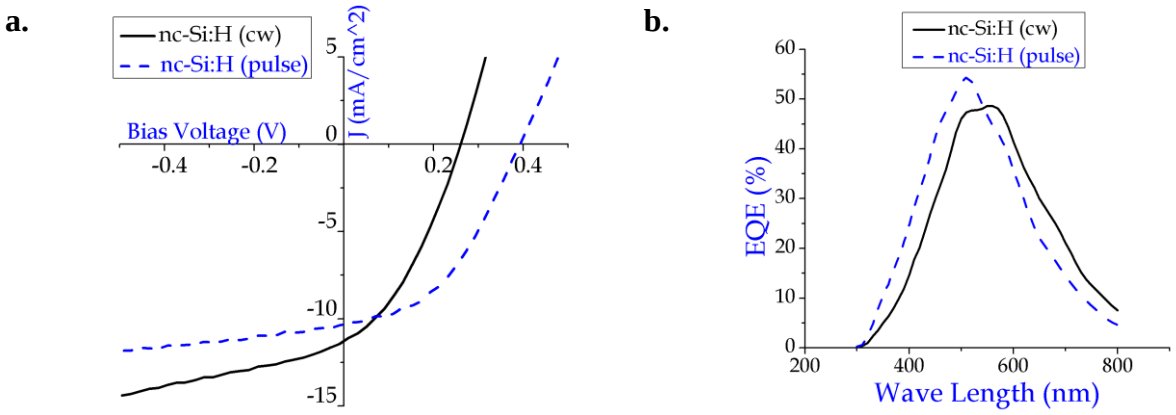

Figure 4.9: The **(a)** J-V curves and **(b)** EQE curves of p-i-n solar cells with 600 nm active layers fabricated from cw and p-PECVD processes respectively.

Two p-i-n solar cell devices were fabricated on SnO_2 coated glass wafers in superstrate configuration. The optimum recipes from both the cw and p-PECVD processes were used to fabricate the 600nm thick cell absorber layers. After the fabrication process, the J-V and the EQE

of the cells were measured. It was observed that the cell with the absorber layer fabricated from the p-PECVD process demonstrated a higher η of 1.7 ± 0.06 % and maximum EQE peak of ~54% compared to that attained from the cw-PECVD process (**Figure 4.9 a** and **b**).

The characteristic solar cell parameters, V_{oc}, J_{sc}, and FF, of the respective solar cells are enlisted in **Table 4.5** (**column 1** and **2**). For comparison purposes the parameters of an 840 nm absorber layer nc-Si:H cell reported by U. Das et al. is also listed (**Table 4.5**; **column 3**) [24]. It was observed that the parameters for both the devices fabricated from cw and p-PECVD were lower than the reported cell.

Table 4.5: The characteristic parameters of the p-i-n cells with 600 nm absorber layers fabricated from cw and p-PECVD. A cell, reported by U. Das et al., with an 840 nm absorber layer fabricated from p-PECVD is also shown for comparison purposes [24].

		1	2	3
		(cw-PECVD) [Annealed]	**(p-PECVD) [Annealed]**	**(p-PECVD) U. Das et al. [24]**
Absorber Layer Thickness		600nm		840nm
1	**V_{oc} (V)**	0.258 ± 0.002	0.388 ± 0.006	~0.5
2	**J_{sc} (mA/cm^2)**	(–) 10.7 ± 0.4	(–) 10.2 ± 0.1	(–) 15–20
3	**FF (%)**	36 ± 0.6	43.0 ± 0.4	65–70
4	**R_{shunt} (Ω)**	316 ± 46	762 ± 96	–
5	**R_{series} (V_{oc} slope; Ω)**	54.3 ± 0.7	72.8 + 0.6	–
6	**Efficiency (%)**	1.00 ± 0.04	1.7 ± 0.06	6–7

4.5.1 Open – circuit Voltage (V_{oc})

The low V_{oc} (**Table 4.5 row 1**) of the cells resulted from the drop in the R_{shunt} (**Table 4.5 row 4**). This occurs when there is an alternate path for current to pass through the cell, mostly around the edges of the cell and between the contacts of different polarity [27]. The lost current is often referred to as the shunt leakage current [34]. It was speculated that the observation of low R_{shunt} originated from two sources:

1. The inadequate electrical isolation of the individual cells
2. The contact of the n – layer (N^+ a-Si:H) with the top contact TCO at the edge of the p-i-n thin film deposition area

This may explain the difference in the V_{oc} of the cw and p-PECVD cells, since it contradicted the nc-Si:H thin film characterization results. This was because, the higher crystallinity of the nc-Si:H films fabricated using p-PECVD was expected to have larger bulk recombination and poor p/i interface, thus resulting in a lower V_{oc} compared to that of the cw-PECVD cell. This was not the case here.

Additionally, the E_A of the p – layer may have been large due to poor doping. High E_A also leads to a decrease in the V_{oc} of the cell. This will be discussed further in the next section.

4.5.2 Short – circuit Current Density (J_{sc})

The low J_{sc} (**Table 4.5 row 2**) was attributed to the following:

1. Poor spectral response, hence low EQE (**Figure 4.9 b**), of the cells at:
    a. *Shorter wavelengths (<450nm)*
    b. *longer wavelengths (>500nm)*
2. High R_{series}

These factors are expounded below:

i. Poor Spectral Response at Shorter Wavelengths (<450nm):

It was speculated that the decrease in the EQE for *shorter wavelengths* (<450nm) resulted from the excessive absorption of high energy photons in the p – layer. This occurs when the p – layer has a significant amorphous to crystalline volume fraction, which may result from the presence of a thicker incubation layer. Since the p – layer was 20nm thick, the fabricated film had to be highly crystalline or else the incubation layer would be too thick.

The presence of a significantly high amorphous volume fraction in the p – layer not only impeded heavy doping but also increased the absorption coefficient of the film at shorter wavelengths [3, 56]. However, these photogenerated carriers, from the increased absorption in

the p – layer, are lost due to the lack of E-field needed for charge collection and high defect density. As a result the EQE steeply dropped in this regime. Furthermore, the p – layer was not efficiently doped due to the amorphous nature of the film, which requires higher concentration of dopant atoms in order to be heavily doped compared to the nc-Si:H thin film doping. Thus it was conjectured that the E_A energy of the p – layer may have been high.

This also decreased the electric field strength in the absorber layer, which led to poor carrier extraction and hence a *low EQE peak height*. Having said that, due to the experimental time constraints, adequate set of characterization experiments were not performed in order to acquire a heavily doped and highly crystalline P^+ nc-Si:H film.

ii. Poor Spectral Response at Longer Wavelengths (>500nm):

The decrease in the EQE for *longer wavelengths* (>500nm) resulted from the fabrication of a thin absorber layer (600nm) and inadequate light trapping. In addition, high concentration of impurities in the absorber layer may have also decreased the long wavelength response of the cell [36, 53]. The high E_A of the nc-Si:H deposited by p-PECVD also suggested the presence of impurities in the cell (**Section 4.4.2**). But the source of the low E_A in the said nc-Si:H film originated from the indiffusion of impurities from the air [36]. However, in a p-i-n device structure the sealing effects of the TCO and the metallic contact layers would minimize this effect on the cell [36]. As a result, if the cell was indeed contaminated, the most likely source of the contaminants would have been from within the deposition chamber, such as *high base pressure, graphite heater* etc.

T. Kilper et al. reported that the critical initial base pressure ranging from 6E-6 to 7E-6 Torr would be the maximum limit for acquiring good quality nc-Si:H films under *air leak conditions* [53]. At this base pressure the critical impurity concentration in the film is reached [53]. Consequently, any rise in the initial base pressure beyond this point would lead to a deterioration of the characteristic solar cell parameters, J_{sc} and FF, due to high impurity concentration [53]. Since the PECVD chamber base pressure was on the order of 1-3E-6 Torr, impurity contamination of the film due to high initial base pressure can be ruled out. Nevertheless, this does not disprove the possibility of film contamination via pure *oxygen* and *nitrogen* in the

plasma. The critical initial base pressures of either of these impurities are in the range of 1-2E-6 Torr. Additionally, carbon from the graphite heater may have contaminated the film during the fabrication process.

Hence, Secondary Ion Mass Spectroscopy (SIMS) characterization measurement needs to be performed in order to identify the type of the impurity present in the absorber layer and quantitatively ascertain their concentration level. Only then can an adequate explanation be made on whether or not the cell J_{sc} and FF were compromised by the presence of the critical concentration of impurities. However, this was beyond the time limit of this research.

iii. High Series Resistance (R_{series}):

The observed high R_{series} (**Table 4.5 row 5**) also led to a decrease in the J_{sc}. It was considered that this arose from the presence of an oxide layer in between the n – layer and the Al contact layer. Prior to the deposition of the Al contact layer the n – layer of the p-i-n cell was exposed to air, which partially oxidized its top surface.

4.5.3 Fill Factor (FF)

Finally, the sum combination of high R_{series} and low R_{shunt} led to a poor FF.

Having said that, the solar cells with absorber layers fabricated from p-PECVD demonstrated a higher η and EQE compared to that of the cw-PECVD cell under the same deposition conditions. However, the aforementioned causes for the observation of poor characteristic parameters, compared to the reported cell, need to be mitigated. Only then can an adequate conclusion be reached on whether the quality of the cell is improved through p-PECVD process or not.

Chapter 5: Conclusion

5.1 Concluding Remarks

In conclusion, the nc-Si:H thin films were fabricated on glass substrates near the a-Si:H to nc-Si:H transition region using cw-PECVD. All the deposition parameters were fixed except for the hydrogen dilution ratio, which was varied from 98% to 99%. Thereafter, the *deposition rate*, *Raman crystallinity*, *I(220)/I(111) XRD peak ratio*, σ_{ph} and σ_D, and *photoresponsivity* of the respective films were measured and compared with respect to each other.

The nc-Si:H film recipe of 98.57% hydrogen dilution ratio was qualitatively chosen based on the optimal showing of the aforementioned parameters. Thereafter, the selected recipe was further subjected to p-PECVD. Six individual samples were deposited at the following pulsing frequencies: 0.2, 1, 5, 10, 25, 50 kHz and duty cycle of 50% respectively. Similar characterization techniques, mentioned above, were then employed to measure and compare the samples. Consequently, the nc-Si:H recipe for 5 kHz pulsing frequency was qualitatively chosen based on the similar selection criterion for the cw-PECVD.

The *deposition rates* of the optimized nc-Si:H thin films from cw and p-PECVD were 0.234 $\pm$ 0.004 Å/s and 0.197 $\pm$ 0.004 Å/s respectively. Additionally, the deposition rate of the p-PECVD nc-Si:H samples were approximately the same regardless of the pulsing frequency, with an average of 0.198 $\pm$ 0.005 Å/s. The lower deposition rate of the p-PECVD samples were related to the turning ON and OFF of the plasma and the associated peak power.

The *Raman crystallinity* and *I(220)/I(111) XRD peak ratio* of the nc-Si:H film deposited at the optimum p-PECVD recipe was 80.8 $\pm$ 0.2 % and 0.58 $\pm$ 0.03 respectively. These values were higher than cw-PECVD values of 71.8 $\pm$ 0.2 % and 0.48 $\pm$ 0.01 respectively. The higher reported values for the p-PECVD sample resulted from the increased generation of the SiH_3 and H species during plasma ON time, due to the higher peak power, and the removal of reactive low lifetime species during the plasma OFF time.

The σ_D of the nc-Si:H thin film deposited from the optimum p-PECVD recipe was 10.0E-04 $\pm$ 2E-05 S/cm compared to 5.4E-04 $\pm$ 4E-05 S/cm obtained from the optimum cw-PECVD recipe. This resulted from the higher crystallinity of the p-PECVD sample. However, the σ_{ph} remained approximately the same for the cw and p-PECVD samples at 1.20E-03 $\pm$ 3E-05 S/cm and 1.40E-03 $\pm$ 3E-05 S/cm respectively. Consequently, the photoresponsivity dropped from 2.23 $\pm$ 0.15 for the cw-PECVD sample to 1.39 $\pm$ 0.02 for the p-PECVD sample. These values were closer to the photoresponsivity values of doped nc-Si:H films, which is approximately close to unity.

Annealing the p-PECVD samples increased their σ_{ph} from 1.40E-03 $\pm$ 3E-05 S/cm to 2.2E-03 $\pm$ 2E-05 S/cm. But the σ_D remained the same, as a result the photoresponsivity increased from 1.39 $\pm$ 0.02 to 2.04 $\pm$ 0.25. Having said that, the σ_{ph} and σ_D, of the nc-Si:H films from the both the processes, were one to two orders and three orders of magnitude higher respectively than the reported results [12]. The E_A measurement was performed on the p-PECVD sample in order to investigate this exceptionally high σ_D for the intrinsic nc-Si:H thin film. A value of 0.16 eV indicated that the nc-Si:H film was contaminated with impurities. It was inferred that the low E_A and high σ_D resulted from the indiffusion of impurities from the air.

After the thin film characterization measurements, the nc-Si:H solar cells with 600nm absorber layers were fabricated from the optimum cw and p-PECVD recipes. There after the J-V and the EQE of the cells were measured. A η of 1.00 $\pm$ 0.04 % and 1.7 $\pm$ 0.06 % along with an EQE peak height of ~49% and ~54% for the cw and p-PECVD cells respectively was observed. Although, the η of nc-Si:H cell fabricated from p-PECVD was slightly higher, it was far below the η, 6% - 7%, of a comparable solar cell [24].

The low η of both the cells compared to the reported cell was related to the low V_{oc}, J_{sc}, and FF. The observation of the low V_{oc} resulted from the low R_{sh}. This stemmed from the inadequate electrical isolation of the individual cells and the contact between the n – layer with the top contact TCO at the edge of the p-i-n thin film deposition area. The low J_{sc} resulted from the insufficient photocarrier collection at longer and shorter wavelengths and high R_{series}. Additionally, the overall effect of the low R_{sh} and high R_{series} led to a poor FF.

5.2 Possible Future Improvements

From the aforementioned brief overview of what was achieved in this research, one may conclude that it is still ambiguous as to which process, cw or p-PECVD, provides a better device quality nc-Si:H film at 150^{o}C substrate temperature. Thus further investigation is required in the following areas:

5.2.1 Thin Film Deposition

1. *Deposition rate* of the nc-Si:H should be increased by using *higher pressures*, *power* and a *smaller electrode distance*. This will allow for the fabrication of thicker films and reduce the overall fabrication time. It was reported that the state of the art nc-Si:H films were deposited in the pressure range of *10-12 Torr* and an electrode gap of *1 cm* [18].
2. ***Substrate temperature*** needs to be precisely measured and maintained below 150^{o}C for the time duration of the deposition process. It was observed that, over the course of the nc-Si:H film deposition time, the temperature rose 30-40^{o}C over the set substrate temperature value of 150^{o}C. Such a rise in substrate temperature during processing may have been related to plasma assisted substrate heating [18]. Experimental measurements revealed that only a small fraction of the overall power is utilized in dissociating and sustaining the plasma, while the rest of the power is dissipated through the chamber walls [18]. Having said that, this may have also resulted from the inadequate temperature calibration results reported in the instrument manual. As a result, this temperature rise needs to be investigated and the initial temperature needs to be adequately set so that the

substrate temperature does not rise above 150^{o}C. This will allow for the proper comparison of the nc-Si:H film structural and electronic properties. Additionally, the optimized recipes can then be easily transferred onto the *plastic substrates*.

3. ***Initial Base Pressure*** should be on the order of 1E-7 to 1E-8 Torr range. The initial base pressure has a direct correlation with the concentration of the impurities incorporated in the deposited film [53]. Hence, if the initial base pressure increases then the impurity concentration in the film rises as well [53]. However, this increase in the impurity concentration does not affect the film structural and electronic properties until a critical limit is reached [53]. This critical limit is different for the initial impurities present within the chamber, such as oxygen, nitrogen, normal air-leak with different admixture of gaseous molecules etc. [53]. The identified critical base pressure for oxygen, nitrogen, and air leak are 1 – 2E-6, 1 – 2E-6, and 6 – 7E-6 Torr respectively [53]. Therefore, the initial base pressure should be *at least* lower than ~1E-6 Torr.
4. ***Stress measurements*** need to be performed in order to investigate the stresses in the nc-Si:H films. During fabrication some 15-20 nc-Si:H films peeled off from the substrate surface after deposition.
5. ***Higher pulsing frequencies*** up to 100 kHz along with different ***duty cycle ratios*** need to be explored in order to investigate the nc-Si:H structural and electronic properties in these regimes. The pulsing frequency above 50 kHz was not investigated because the peak power was not high enough. When the plasma is turned ON from OFF the applied power overshoots and it takes a certain amount of time for the applied power to decrease to the specified peak power. Thus for smaller peak powers the time required for the power to decrease is longer. As a result, the pulse duration ($\tau_{duration}$) needs to be longer in order to allow the power to decrease to the specified peak power. This results in a ceiling frequency (duty cycle is constant) above which the power will not drop fast enough to reach the specified peak power. As a consequence in order to explore higher pulsing frequencies up to 100 kHz a ***higher average power*** is required.

5.2.2 Thin Film Characterization Measurements

1. ***Raman measurement*** needs to be performed on nc-Si:H films that have the same thickness as the cell absorber layer. This is because nc-Si:H microstructure varies with thickness [54]. Additionally, the p – layer in thin film solar cell acts as the crystalline seed layer for the nc-Si:H absorber layer growth. Hence the microstructure of the nc-Si:H absorber layer film is different compared to that grown on glass wafers. As a result, in order to simulate the microstructure of the cell absorber layer the Raman measurements should be performed on nc-Si:H films with a predeposited seed layer. Additionally, 100nm thick chromium film should be deposited before the initial seed layer is deposited so that the Raman back scattered photon contribution from the glass substrate is cut off [54].
2. ***Coplanar conductivity*** measurement should be performed within a day of the nc-Si:H film deposition or else the atmospheric indiffusion of H_2O, O_2, or N_2 will significantly increase the σ_D and decrease the E_A of the film [36, 53].
3. ***SIMS*** measurement needs to be performed on the nc-Si:H films deposited in the Reel to Reel PECVD chamber. The obtained results would further help to determine the cause behind the observation of the poor solar cell characteristic parameters.
4. ***Microstructural growth*** needs to be further studied using TEM measurements. Furthermore, the ***optical properties*** of nc-Si:H fabricated via cw and p-PECVD have been wholly overlooked in this research and need to be further investigated in order to understand the influence of the pulsing frequency on the electronic and photonic bandgap, absorption coefficient etc. of the deposited nc-Si:H films.

5.2.3 Solar Cell Fabrication

1. ***Absorber layer*** thickness should be 1-2 µm. The 600nm absorber layer, used in this research, led to poor absorption at longer wavelengths.
2. ***P – layer*** needs to be properly characterized for adequate ***doping and crystallinity***.
3. ***ZnO TCO layer*** is a better alternative for the top contact instead of the SnO_2 TCO layer used in this study. This is because it has higher transmittance at longer wavelengths.

4. ***Cell area*** of should be increased from 0.25 cm^2 to 1 cm^2. This would greatly reduce the lateral collection of the photogenerated current from the adjoining areas, regions not directly under the back electrode, of the solar cell.
5. ***Electrical isolation*** of the cells is required in order to prevent R_{sh}. This is achieved by etching the edges of the p-i-n deposition area and the adjoining n – layer around the cell.

A more rigorous comparison of the structural and electronic properties of the nc-Si:H films deposited via both cw and p-PECVD processes can be achieved once the aforementioned improvements are implemented and the prospective research areas are investigated. Additionally, the solar cell characteristic parameters fabricated from both the processes can be adequately compared as well. The obtained results from the aforementioned studies will then indicate whether or not, p-PECVD process improves the structural and electronic quality of the deposited nc-Si:H film and contributes toward improving the efficiency of the nc-Si:H solar cells on flexible substrates at low temperatures.

References

[1] M. A. Green, K. Emery, Y. Hishikawa, and W. Warta, "Solar Cell Efficiency Tables (Version 32)," *Progress in Photovoltaics*, vol. 16, no. 5, pp. 435 – 440, Aug. 2008.

[2] B. Rech, T. Roschek, T. Repmann, J. Muller, R. Schmitz, and W. Appenzellar, "Microcrystalline silicon for large area thin film solar cells," *Thin Solid Films*, vol. 427, no. 1 – 2, pp. 157 – 165, Mar. 2003.

[3] A. Sazonov, ECE 730. Class Notes, Topic: "Amorphous, Nanocrystalline, and Polycrystalline Silicon," Department of Electrical and Computer Engineering, University of Waterloo, Waterloo, Ontario, 2008.

[4] R. E. I. Schropp and M. Zeman, *Amorphous and Microcrystalline Silicon Solar Cells: Modelling, Materials and Device Technology*. Norwell, MA: Kluwer Academic Publishers, 1998, pp. 3 – 6.

[5] A. V. Shah, H. Schade, M. Vanecek, J. Meier, E. Vallat-Sauvain, N.Wyrsch, U. Kroll, C. Droz and J. Bailat, "Thin-film Silicon Solar Cell Technology," *Progress In Photovoltaics: Research and Application*, vol. 12, no. 2 – 3, pp. 113 – 142, Mar. 2004.

[6] S. Guha, "Multijunction Solar Cells and Modules," in *Technology and Applications of Amorphous Silicon*, R. A. Street, Ed. Germany: Springer, 2000, pp. 252 – 305.

[7] X. Deng and E. A. Schiff, "Amorphous Silicon-based Solar Cells," in *Handbook of Photovoltaic Science and Engineering*, 1st ed., A. Luque and S. Hegedus, Ed. England: John Wiley and Sons, 2003, pp. 505 – 565.

[8] H. J. Moller, *Semiconductors for Solar Cells*. Norwood, MA: Artech House, 1993, pp. 12, 21 & 331.

[9] A. Matsuda, “Formation Kinetics and Control of Microcrystallite in μc-Si:H from Glow Discharge Plasma,” *Journal of Non-Crystalline Solids*, vol. 59 & 60, no. 2, pp. 767 – 774, Dec. 1983.

[10] J. Meier, S. Dubali, R. Platz, P. Torres, U. Kroll, J. A. Anna Selvan, N. Pellaton Vaucher, Ch. Hof, D. Fischer, H. Keppner, R. Fluckiger, A. Shah, V. Shklover, and K. D. Ufert, “Towards high-efficiency thin-film silicon solar cells with the ‘micromorph” concept,” *Solar Energy Materials and Solar Cells*, vol. 49, no. 1 – 4, pp. 35 – 44, Dec. 1997.

[11] M. Zeman, “Advanced Amorphous Silicon Solar Cell Technologies,” in *Thin Film Solar Cells: Fabrication, Characterization, and Application*, 1st ed., J. Poortmans and V. Arkhipov, Ed. England: John Wiley and Sons, Jan. 2007, pp. 173 – 236.

[12] O.Vetterl, F. Finger, R. Carius, P. Hapke, L. Houben, O. Kluth, A. Lambertz, A. Muck, B. Rech, and H. Wagner, “Intrinsic microcrystalline silicon: A new material for photovoltaics”, *Solar Energy Materials and Solar Cells*, vol. 62, no. 1 – 2, pp 97 – 108, Apr. 2000.

[13] L. Houben, M. Luysberg, P. Hapke, R. Carius, F. Finger, and H. Wagner, “Structural properties of microcrystalline silicon in the transition from highly crystalline to amorphous growth,” *Philosophical Magazine A – Physics of Condensed Matter Structure, Defects, and Mechanical Properties*, vol. 77, No. 6, pp. 1447 – 1460, Jun. 1998.

[14] A. Matsuda, “Amorphous and Microcrystalline Silicon,” in *Springer Handbook of Electronic and Photonic Materials*, S. Kasap and P. Capper, Ed., Springer US, July 2007, pp. 581 – 595.

[15] J. R. Sheats, “Roll-to-roll manufacturing of thin film electronics,” in *Proceedings of SPIE: Emerging Lithographic Technologies VI*, R. L. Engelstad, Ed. vol. 4688, 2002, pp. 240 – 248.

[16] L. Guo, M. Kondo, M. Fukawa, K. Saitoh, and A. Matsuda, “High Rate Deposition of Microcrystalline Silicon Using Conventional Plasma-Enhanced Chemical Vapor Deposition,” *Japanese Journal of Applied Physics Part 2 – Letters*, vol. 37, no. 10A, pp L1116 – L1118, Oct. 1998.

[17] W. G. J. H. M. van Sark, G. W. Brandsen, M. Fleuster, and M. P. Hekkert, “Analysis of the silicon market: Will thin films profit?,”*Energy Policy*, vol. 35, no. 6, pp. 3121 – 3125, June 2007.

[18] M. N. van den Donker, B. Rech, R. Schmitz, J. Klomfass, G. Dingemans, F. Finger, L. Houben, W. M. M. Kessels, and M. C. M. V. de Sanden, “Hidden parameters in the plasma deposition of microcrystalline silicon solar cells,” *Journal of Materials Research*, vol. 22, no.7, pp. 1767 – 1774, July 2007.

[19] M. Kondo, M. Fukawa, L. Guo, and A. Matsuda, “High rate growth of microcrystalline silicon at low temperatures,” *Journal of Non-Crystalline Solids*, vol. 266, Part A, pp. 84 – 89, May 2000.

[20] C. Niikura, M. Kondo, and A. Matsuda, “High rate growth of microcrystalline silicon films assisted by high density plasma,” in *3rd World Conference on Photovoltaic Energy Conversion*, vol. A – C, May 2003, pp. 1710 – 1713.

[21] T. Roschek, T.Repmann, J. Muller, B. Rech, and H. Wagner, “Comprehensive study of microcrystalline silicon solar cells deposited at high rate using 13.56 MHz plasma-enhanced chemical vapor deposition,” *Journal of Vacuum Science and Technology A*, vol. 20, no. 2, pp. 492 – 498, Mar. 2002.

[22] Ch. Hollenstein, “The physics and chemistry of dusty plasmas,” *Plasma Physics and Controlled Fusion*, vol. 42, no. 10, pp. R93 – R104, Oct. 2000.

[23] A. A. Howling, L. Sansonnens, J. L. Dorier, and Ch. Hollenstein, "Time-resolved measurements of highly polymerized negative ions in radio frequency silane plasma deposition experiments," *Journal of Applied Physics*, vol. 75, no. 3, pp. 1340 – 1353, Feb. 1994.

[24] U. Das, S. Morrison, E. Centurioni, and A. Madan, "Thin film silicon materials and solar cells grown by pulsed PECVD technique," in *IEE Proceedings – Circuits Devices and Systems*, vol. 150, no. 4, Aug. 2003, pp. 282 – 286.

[25] U. K. Das, S. Morrison, and A. Madan, "Amorphous and Microcrystalline Silicon Solar Cells Grown by Pulsed PECVD Technique," in *Materials Research Society Symposium Proceedings*, vol. 715, Apr. 2002, pp. 611 – 616.

[26] J. Perrin, "Reactor Design for a-Si:H Deposition," in *Plasma Deposition of Amorphous Silicon – Based Materials*, 1st ed., G. Bruno, P. Capezzuto, and A. Madan, Ed. San Diego: Academic Press, 1995, pp. 177 – 237.

[27] J. Nelson, *The Physics of Solar Cells*. London, UK: Imperial College Press, 2007, pp. 51 – 53.

[28] D. A. Neamen, *Semiconductor Physics and Devices*. New York, NY: Mcgraw-Hill, 2003, pp. 83 – 86.

[29] E. Schiff, "Device Physics of Nanocrystalline (and Amorphous) Silicon Solar Cells," National Renewable Energy Laboratory, Apr. 17, 2006. [Online]. Available: www.nrel.gov/pv/thin_film/docs/asi06schi.ppt. [Accessed: May 10, 2010].

[30] T. Dylla, F. Finger, and E. A. Schiff, "Hole drift-mobility measurements in microcrystalline silicon," *Applied Physics Letters*, vol. 87, no. 3, pp. 032103 1 – 3, July 2005.

[31] M. M. Adachi, “Low Temperature Thin Film Silicon Solar Cells Prepared by Hot-Wire Chemical Vapor Deposition,” M. S. Thesis, Simon Fraser University, Vancouver, BC, Canada, 2007.

[32] H. J. Lee, “Top Gate Nanocrystalline Silicon Thin Film Transistors,” M. S. Thesis, University of Waterloo, Waterloo, ON, Canada, 2008

[33] T. Kamei, T. Wada, and A. Matsuda, “Effects of oxygen impurity on microcrystalline silicon films,” in *Conference Record of the Twenty-Eighth IEEE Photovoltaic Specialists Conference – 2000*, vol. 28, Sep. 2000, pp. 784 – 787.

[34] Y. Nasuno, M. Kondo, and A. Matsuda, “Passivation of oxygen-related donors in microcrystalline silicon by low temperature deposition,” *Applied Physics Letters*, vol. 78, no. 16, pp. 2330 – 2332, Apr. 2001.

[35] C. Honsberg and S. Bowden, “Chap. 4: Solar Cell Operation,” Solar Power Labs at Arizona State University (ASU). [Online]. Available: http://pvcdrom.pveducation.org/. [Accessed: May 10, 2010].

[36] A. V. Shah, J. Meier, E. Vallat-Sauvain, N. Wyrsch, U. Kroll, C. Droz, and U. Graf, “Material and solar cell research in microcrystalline silicon,” *Solar Energy Materials and Solar Cells*, vol. 78, no. 1 – 4, pp. 469 – 491, 2003.

[37] R-2-R manual, *Reel to Reel Cassette system: Plasma Enhanced Chemical Vapor Deposition (PECVD) Chamber, Dual Sputter Cathode Chamber and Load Lock*, MVSystems, 2006.

[38] C. H. Lee, “Nanocrystalline Silicon Thin Film Transistors,” M. S. Thesis, University of Waterloo, Waterloo, ON, Canada, 2008

[39] H. Kakinuma, M. Mohri, M. Sakamoto, and T. Tsuruoka, "Structural properties of polycrystalline silicon films prepared at low temperature by plasma chemical vapor deposition," *Journal of Applied Physics*, vol. 70, no. 12, pp. 7374 – 7381, Dec. 1991.

[40] T. Okada, T. Iwaki, H. Kasahara, and K. Yamamoto, "Probing the crystallinity of Evaporated Silicon Films by Raman Scattering," *Japanese Journal of Applied Physics*, vol. 24, no. 2, pp. 161 – 165, Feb.1985.

[41] H. Keppner, J. Meier, P. Torres, D. Fischer, and A. Shah, "Microcrystalline silicon and micromorph tandem solar cells," *Applied Physics A – Materials Science & Processing*, vol. 69, no. 2, pp. 169 – 177, Aug. 1999.

[42] "Bragg's Law," [Online]. Available: http://en.wikipedia.org/wiki/Bragg's_law. [Accessed: May 10, 2010].

[43] Scintag, Inc. "Chapter 7: Basics of X-ray Diffraction," Department of Earth and Planetary Sciences at University of New Mexico (UNM). [Online]. Available: http://epswww.unm.edu/xrd/xrdbasics.pdf. [Accessed: May 10, 2010].

[44] H & M Analytical Services Literature, "Grazing Incidence Angle Thin Film Analysis," H & M Analytical Services, Inc. [Online]. Available: http://www.h-and-m-analytical.com/pdfs/grazing_incidence.pdf. [Accessed: May 10, 2010].

[45] Sergey Stepanov, "Grazing Incidence X-ray Diffraction", in *3rd Autumn School on X-ray Scattering from Surfaces and Thin Layers*, Smolenice, Slovakia. Oct.1997.

[46] B. K. Tanner, T. P. A. Hase, T. A. Lafford, and M. S. Goorsky, "Grazing Incidence in-plane X-ray diffraction in the laboratory," in *Powder Diffraction*, vol. 19, no. 1, Mar. 2004, pp. 45 – 48.

[47] P. Dutta, “Grazing incidence X-ray diffraction,” *Current Science,* Vol. 78, no. 12, pp. 1478 – 1483, June 2000.

[48] E. Vallat-Sauvain, A. Shah, and J. Bailat, “Advances in Microcrystalline Silicon Solar Cell Technologies,” in *Thin Film Solar Cells: Fabrication, Characterization, and Application,* 1st ed., J. Poortmans and V. Arkhipov, Ed. England: John Wiley and Sons, Jan. 2007, pp. 133 – 171.

[49] E. Vallat-Sauvin, U. Kroll, J. Meier, J. Pohl, and A. Shah, “Evolution of the microstructure in the microcrystalline silicon prepared by very high frequency glow-discharge using hydrogen dilution,” *Journal of Applied Physics,* vol. 87, no. 6, pp. 3137 – 3142, Mar. 2000.

[50] Y. Sun, T. Miyasato, and J. K. Wigmore, “Possible origin for (110)-oriented growth of grains in hydrogenated microcrystalline silicon films,” *Applied Physics Letters,* vol. 70, no. 4, pp. 508 – 510, Jan. 1997.

[51] Bruno, P. Capezzuto, and G. Cicala, “Chemistry of Amorphous Silicon Deposition Process,” in *Plasma Deposition of Amorphous Silicon – Based Materials,* 1st ed., G. Bruno, P. Capezzuto, and A. Madan, Ed. San Diego: Academic Press, 1995, pp. 47.

[52] S. Wang, X. Zhang, Y. Zhao, C. Wei, S. Xu, J. Sun, and X. Geng, “Effects of modulation frequency on the structure and electrical characteristics of μc-Si:H films prepared by pulsed VHF PECVD,” *Optoelectronics Letters,* vol. 5, no. 3, pp. 212 – 215, May 2009.

[53] T. Kilper, W. Beyer, G. Brauer, T. Bonger, R. Carius, M. N. van den Donker, D. Hrunski, A. Lambertz, T. Merdzhanova, A. Muck, B. Rech, W. Reetz, R. Scmitz, U. Zastrow, and A. Gordijn, “Oxygen and nitrogen impurities in microcrystalline silicon deposited under optimized conditions: Influence on material properties and solar cell performance,” *Journal of Applied Physics,* vol. 105, pp. 074509 1 – 10, Apr. 2009.

[54] J. Kocka, H. Stucklikova, J.Stuchlik, B. Rezek, T. Maters, V. Svrcek, P. Fojtik, I. Pelant, and A. Fejfar, “Model of transport in microcrystalline silicon,” *Journal of Non-Crystalline Solids*, vol. 299-302, pp. 355-359, 2002.

[55] Y. Toyoshima, K. Arai, and A. Matsuda, “Lattice orientation of microcrystallites in μc-SiH,” *Journal of Non-Crystalline Solids*, vol. 114, no. 2, pp. 819 – 821, Dec. 1989.

[56] Y. Tawada, K. Tsuge, M. Kondo, H. Okamoto, and Y. Hamakawa, “Properties and Structure of a-SiC:H for high efficiency a-Si cell,” *Journal of Applied Physics*, vol. 53, no. 7, pp. 5273 – 5281, Jul. 1982.

Appendix

Phase 1: Fabricating nc-Si:H in cw-PECVD at 150ºC substrate temp. on glass subs.

Goal:

1. Deposit nanocrystalline thin films using cw-PECVD and measure DR.
2. Produce R (220) vs. [H_2] ratio plot.
3. Get GUR (Gas utilization ratio)

Mohammad's Recipe (WL01):

1. Power: 2W
2. Pressure: 0.9 Torr
3. H_2: 200sccm
4. SiH_4: 2sccm
5. T_H: 400C (Ts: 280C)
6. Electrode Distance: (1.5cm - 2 cm)
7. Electrode area: 18 cm x 18 cm (outside), 16.5 cm x 16.5 cm
8. Approximate Volume of the PECVD chamber (*Height:* 25cm-0.5cm-0.5cm=24cm; *Length:* 25cm-0.5cm-0.5cm=24cm; *Width:* 25cm-0.5cm-0.5cm=24cm): **13,824 cm^3**

Fixed Parameters (CW, plasma freq. 13.56 MHz – Reel to Reel):

1. **Substrate Temp.:** $150 \pm 20\ ^{\circ}C$ (**Heater Well (T_H):** $250 \pm 20\ ^{\circ}C$, **Graphite Heater (T_G):** $250 \pm 10\ ^{\circ}C$, soaking period of **1hr.**)
2. **Electrode Distance:** 1.93 ± 0.06 cm
3. **Deposition Pressure:** 1000 ± 2 mTorr
4. **Electrode Area:** 15cm (w) x 15cm (L) (~15.5cm)
5. **Approximate Volume of the PECVD chamber** (*Height:* 50.5cm-1.5cm=49cm; *Length:* 47.5cm-3cm=44.5cm; *Width:* 49.5cm-3cm=46.5cm): **101,393.25 cm^3**
6. **[SiH_4]:** 2 sccm [1.9 ± 0.1]**(fixed, MFC SiH_4 limit is 100sccm; upper limit** $\left[\frac{2sccm \times 101393.25cm^3}{13824cm^3} = 14.67sccm \approx 15sccm\right]$)
7. **Variable:** H_2 flow rate.

1. **Power:** 2 ± 0.05 W (Initial Ignition Power ~3.5W), **Time:** 30 min

Sample	[H_2] flow rate (sccm), with [SiH_4] flow rate of 2 sccm	Hydrogen Dilution Ratio $\left(\frac{[H_2]}{[H_2]+[SiH_4]}\right)$	Sample Phase (Checked using Raman Spectroscopy)
Sam001*	18 ± 3	90%	Amorphous
Sam002	23 ± 3	92%	Amorphous
Sam003	48 ± 3	96%	Amorphous
Sam004	98 ± 3	98%	Amorphous
Sam005	150 ± 3	98.7%	Crystalline (58.0 $\pm$ 3.0 %)
Sam006	200 ± 3	99%	Crystalline (70.5 $\pm$ 0.9 %)

*** Sam001 had a deposition time of 60 minutes**

Power: 5 ± 0.05 W, **Time:** 2hr

Sample	$[H_2]$ flow rate (sccm), with $[SiH_4]$ flow rate of 2 sccm	Hydrogen Dilution Ratio	Sample Phase	Film Thickness (Å)	Deposition Rate (Å/s)	**Time** Required to Deposit 300nm film (s)/hrs
Sam007 (a & b)	98.0 ± 3	98.00%	Amorphous	2188 ± 25	0.303 ± 0.004	9,901s (2hrs 45mins 1s)
Sam012 (a & b)	112.5 ± 3	98.25%	Crystalline	1995 ± 28	0.277 ± 0.004	10,830s (3hrs 0mins 30s)
Sam008 (a & b)	125.0 ± 3	98.43%	Crystalline	1815 ± 45	0.252 ± 0.006	11,905s (3hrs 18mins 25s)
Sam013 (a & b)	137.5 ± 3	98.57%	Crystalline	1687 ± 29	0.234 ± 0.004	12,821s (3hrs 33mins 41s)
Sam009 (a & b)	150.0 ± 3	98.68%	Crystalline	1589 ± 26	0.22 ± 0.004	13,636s (3hrs 47mins 16s)
Sam010 (a & b)	175.0 ± 3	98.87%	Crystalline	1400 ± 10	0.194 ± 0.001	15,464s (4hrs 17mins 44s)
Sam011 (a & b)	200.0 ± 3	99.01%	Crystalline	1156 ± 22	0.16 ± 0.003	18,750s (5hrs 12mins 30s)

Thickness: 300 nm

Sample	Hydrogen Dilution Ratio	Sample Crystallinity (Two Peak Method)	Peak Height Ratio I(220)/I(111)	σ_D (S/cm)	σ_{ph} (S/cm)	Photoresponsivity
Sam014 (a & b)	98.25%	62.2 ± 1.1 %	0.39 ± 0.02	4.8E-05 ± 2-06	1.17E-04 ± 5E-06	2.44 ± 0.07
Sam015 (a & b)	98.43%	69.5 ± 0.8 %	0.47 ± 0.02	N/A	N/A	N/A
Sam016 (a & b)	98.57%	71.8 ± 0.2 %	0.48 ± 0.01	5.4E-04 ± 4E-05	1.20E-03 ± 3E-05	2.23 ± 0.15
Sam017 (a & b)	98.68%	69.7 ± 0.8 %	0.46 ± 0.02	7.9E-04 ± 2E-05	1.71E-03 ± 5E-05	2.18 ± 0.08
Sam018 (a & b)	98.87%	68.4 ± 0.5 %	0.42 ± 0.02	8.9E-04 ± 9E-05	1.57E-03 ± 7E-05	1.78 ± 0.14
Sam019 (a & b)	99.01%	65.4 ± 0.6 %	0.38 ± 0.02	9.6E-04 ± 6E-05	1.74E-03 ± 1E-05	1.82 ± 0.19

a-Si:H Test sample:

Recipe:

1. Power: 1.75W
2. Pressure: 400 mTorr
3. SiH_4: 20sccm
4. $T_{Heater\ Well}$ and $T_{Graphite\ Heater}$: 250 ± 20 ^{0}C and 250 ± 10 ^{0}C (Ts: 150 ^{0}C)
5. Electrode Distance: 1.93 ± 0.06 cm
6. Electrode area: 15cm (w) x 15cm (L) (~15.5cm)
7. Time: 35 mins

Sample	Hydrogen Dilution Ratio	σ_D (S/cm)	σ_{ph} (S/cm)	Photoresponsivity
Test	0%	3.1036E-10	2.69166E-05	8.6727E+04 (~E+05)

Deposition surface: non-TCO coated glass (Amorphous), Corning Eagle 2000 Glass

Measurement Techniques:

1. Raman (Randy)
2. Check Deposition Rate (Profilometer, *once the aforementioned recipe is perfected*)
3. XRD (220 orientation is preferred) (Tong Leung's Group)

Tasks:

1. Investigate why the photo/dark conductivity ratio is low?
2. Find papers relating to conductivity measurements.
3. Find papers that talk about the affect of the top conducting p – layer on the i – layer Crystallinity

Phase 2: Fabricating nc-Si:H in p-PECVD at 150ºC substrate temp. on glass subs.

Recipe from Phase 1:

8. **Substrate Temp.:** $150 \pm 20\ ^{\circ}C$ (**Heater Well (T_H):** $250 \pm 20\ ^{\circ}C$, **Graphite Heater (T_G):** $250 \pm 10\ ^{\circ}C$, soaking period of **1hr.**)
9. **Electrode Distance:** 1.93 ± 0.06 cm
10. **Deposition Pressure:** 1000 ± 2 mTorr
11. **Electrode Area:** 15cm (w) x 15cm (L) (~15.5cm)
12. **[SiH_4]:** 2 sccm [1.9 ± 0.1] (**fixed, MFC SiH_4 limit is 100sccm; upper limit** $\left[\frac{2sccm \times 101393.25cm^3}{13824cm^3} = 14.67sccm \approx 15sccm\right]$)
13. **[H_2]:** 137.5 sccm

Also,

14. **Pusling Frequency Lower Limit (instant ignition):** 120 Hz (**Without instant ignition:** 55Hz)
15. **Pulsing Frequency Upper Limit (before incident peak power of the pulse increases beyond the specified peak pulse power):** 55kHz
16. **Duty cycle:** 50%

Deposition time: 1.5 hrs

Sample	Pulse Frequency (kHz)	Pulse Period (µs)	Crystallinity	Film Thickness (Å)	Deposition Rate (Å/s)	**Time** Required to Deposit 300nm film (s)/hrs
Sam013 (a & b)	-	-	Crystalline	-	0.234 ± 0.004	12,821s (3hrs 33mins 41s)
Sam020 (a & b)	0.2 (200Hz)	5000 (5ms)	Crystalline	1068 ± 37	0.198 ± 0.007	15,152s (4hrs 12mins 32s)
Sam021 (a & b)	1	1000 (1ms)	Crystalline	1076 ± 37	0.199 ± 0.007	15,075s (4hrs 11mins 15s)
Sam022 (a & b)	5	200	Crystalline	1062 ± 23	0.197 ± 0.004	15,228s (4hrs 13mins 48s)
Sam023 (a & b)	10	100	Crystalline	1081 ± 17	0.200 ± 0.003	15,000s (4hrs 10mins 00s)
Sam024 (a & b)	25	40	Crystalline	1046 ± 35	0.194 ± 0.006	15,464s (4hrs 17mins 44s)
Sam025 (a & b)	50	20	Crystalline	1062 ± 23	0.197 ± 0.004	15,228s (4hrs 13mins 48s)
Avg. D.R./Time	-	-	-	-	**0.198 ± 0.005**	**15,191s (4hrs 13mins 11s)**

Film Thickness: 300nm (**Approx. Time:** 4hrs 13mins; **15,180 sec**)

Sample	Pulse Frequency (kHz)	Sample Crystallinity (Two Peak Method)	Peak Height Ratio I(220)/ I(111)	σ_D (S/cm)	σ_{ph} (S/cm)	Photoresponsivity
Sam016 (a & b)	-	71.8 ± 0.2 %	0.48 ± 0.01	5.4E-04 ± 4E-05	1.20E-03 ± 3E-05	2.23 ± 0.15
Sam020 (c & d)	0.2 (200Hz)	77.2 ± 0.3 %	0.54 ± 0.04	7.7E-04 ± 5E-05	1.02E-03 ± 7E-05	1.32 ± 0.02
Sam021 (c & d)	1	80.5 ± 0.2 %	0.60 ± 0.03	12.9E-04 ± 3E-05	1.64E-03 ± 8E-05	1.28 ± 0.03
Sam022 (c & d)	5	80.8 ± 0.2 %	0.58 ± 0.03	10.0E-04 ± 2E-05	1.40E-03 ± 3E-05	1.39 ± 0.02
Sam023 (c & d)	10	80.9 ± 0.4 %	0.53 ± 0.03	10.2E-04 ± 3E-05	1.49E-03 ± 10E-05	1.46 ± 0.07
Sam024 (c & d)	25	79.4 ± 0.2 %	0.59 ± 0.03	9.8E-04 ± 2E-05	1.44E-03 ± 3E-05	1.48 ± 0.01
Sam025 (c & d)	50	80.6 ± 0.2 %	0.64 ± 0.04	9.9E-04 ± 2E-05	1.34E-03 ± 5E-05	1.35 ± 0.02

Film Thickness: 300nm (**Approx. Time:** 4hrs 13mins; **15,180 sec**)
Avg. Vacuum Annealing Time at 150 ºC: 22,300 ± 750 sec = **6hrs 12 mins ± 12.5mins**
Vacuum Cool Down Time: 7,980 ± 511 = **2hrs 13 mins + 8.5 mins**

Sample	Pulse Frequency (kHz)	σ_D (S/cm)	**Annealed σ_D (S/cm)**	σ_{ph} (s/cm)	**Annealed σ_{ph} (S/cm)**	Photoresponsivity	**Annealed Photoresponsivity**	**Activation Energy (eV) ***
Sam016 (a & b)	-	5.4E-04 ± 4E-05	-	1.20E-03 ± 3E-05	-	2.23 ± 0.15	-	-
Sam020 (c & d)	0.2	7.7E-04 ± 5E-05	**7.5E-04 ± 8E-05**	1.02E-03 ± 7E-05	**1.5E-03 ± 2E-05**	1.32 ± 0.02	**1.97 ± 0.37**	**0.1524**
Sam021 (c & d)	1	12.9E-04 ± 3E-05	**12.4E-04 ± 3E-05**	1.64E-03 ± 8E-05	**1.71E-03 ± 1E-05**	1.28 ± 0.03	**1.38 ± 0.07**	**0.1393**
Sam022 (c & d)	5	10.0E-04 ± 2E-05	**10.7E-04 ± 3E-05**	1.40E-03 ± 3E-05	**2.2E-03 ± 2E-05**	1.39 ± 0.02	**2.04 ± 0.25**	**0.1432**
Sam023 (c & d)	10	10.2E-04 ± 3E-05	**10.6E-04 ± 9E-05**	1.49E-03 ± 10E-05	**2.0E-03 ± 4E-05**	1.46 ± 0.07	**1.94 ± 0.46**	**0.1630**
Sam024 (c & d)	25	9.8E-04 ± 2E-05	**10.8E-04 ± 4E-05**	1.44E-03 ± 3E-05	**1.6E-03 ± 6E-05**	1.48 ± 0.01	**1.49 ± 0.01**	**0.1676**
Sam025 (c & d)	50	9.9E-04 ± 2E-05	**5.4E-04 ± 2E-05**	0.72E-03 ± 3E-05	**0.94E-03 ± 9E-05**	1.62 ± 0.04	**1.73 ± 0.10**	**0.1682**

Average Actiation: 0.16 ± 0.01 eV
*In order to determine the activation energy, the temperature dependent Conductivity Measurements were performed at three different temperatures, namely **25 ºC, 50 ºC, 75 ºC (298.15 K, 323.15 K, 348.15 K)** respectively.

Goal:

1. Obtain nanocrystalline Thin film using Pulsed Modulated PECVD
2. Produce R (220) vs. [H_2] ratio plot.
3. Measure the Dark, Photo – conductivity of the films.
4. Measure Crystallinity of the samples using Raman spectroscopy.

Tasks:

4. Investigate the **upper** and **lower** limits of pulsing frequency
5. Investigate **high σ_D**